Electronic Supplementary Information (ESI)

A bioinspired thiolate-bridged dinickel complex with a pendant amine: synthesis, structure and electrocatalytic properties

Puhua Sun,[a] Dawei Yang,*[a] Ying Li,[a] Baomin Wang[a] and Jingping Qu*[ab]

[a]*State Key Laboratory of Fine Chemicals, Dalian University of Technology, Dalian 116024, P. R. China.*
[b]*Key Laboratory for Advanced Materials, East China University of Science and Technology, Shanghai, 200237, P. R. China.*

E-mail: qujp@dlut.edu.cn
yangdw@dlut.edu.cn

Contents:

X-ray crystallographic information

Table S1. Crystallographic data for **1[BPh$_4$]$_2$**, **2[PF$_6$]$_2$**·2CH$_2$Cl$_2$

	1[BPh$_4$]$_2$	**2[PF$_6$]$_2$**·2CH$_2$Cl$_2$
Formula	$C_{104}H_{96}B_2Ni_2P_4S_3$	$C_{64}H_{65}Cl_4F_{12}NNi_2P_6S_2$
Formula weight	1704.90	1585.33
Crystal dimensions (mm^3)	0.28 × 0.25 × 0.23	0.30 × 0.28 × 0.25
Crystal system	Monoclinic	Monoclinic
Space group	P 21/c	P2(1)/n
a (Å)	28.1408(18)	13.2896(7)
b (Å)	13.9434(9)	35.8764(18)
c (Å)	25.5790(17)	14.5814(7)
α (º)	90.00	90.00
β (º)	106.097(2)	97.5201(11)
γ (º)	90.00	90.00
Volume (Å^3)	9643.1(11)	6892.4(6)
Z	4	4
T (K)	220(2)	173(2)
D_{calcd} (g cm^{-3})	1.174	1.528
μ (mm^{-1})	0.566	0.974
F (000)	3576	3240
No. of rflns. collected	178329	96297
No. of indep. rflns. /R_{int}	16979 / 0.0393	12126 / 0.0554
No. of obsd. rflns. [$I_0 > 2\sigma(I_0)$]	13776	10037
Data / restraints / parameters	16979 / 0 / 916	12126 / 132 / 929
R_1 / wR_2 [$I_0 > 2\sigma(I_0)$][a]	0.0500 / 0.1158	0.0461 / 0.1065
R_1 / wR_2 (all data)[a]	0.0662 / 0.1227	0.0604 / 0.1118
GOF (on F^2)[a]	1.042	1.030
Largest diff. peak and hole (e Å^{-3})	1.125 / −0.599	0.953 / −0.618

Table S2. Crystallographic data for **3[PF$_6$]**·MeCN, **4[PF$_6$]**·CH_2Cl_2

	3[PF$_6$]·MeCN	**4[PF$_6$]**·CH_2Cl_2
Formula	$C_{58}H_{59}ClF_6Ni_2NP_5S_3$	$C_{57}H_{58}Cl_3F_6Ni_2OP_5S_2$
Formula weight	1287.96	1315.77
Crystal dimensions (mm^3)	0.30 × 0.20 × 0.18	0.28 × 0.27 × 0.25
Crystal system	Monoclinic	Monoclinic
Space group	C2/c	C2/c
a (Å)	35.436(4)	35.7408(15)
b (Å)	13.4228(15)	13.3259(5)
c (Å)	24.186(3)	24.6081(10)
α (º)	90.00	90.00
β (º)	91.00	91.220(3)
γ (º)	90.00	90.00
Volume ($Å^3$)	11502(2)	11717.6(8)
Z	8	8
T (K)	173(2)	230(2)
D_{calcd} (g cm^{-3})	1.488	1.492
μ (mm^{-1})	1.008	1.046
F (000)	5312	5408
No. of rflns. collected	77349	138914
No. of indep. rflns. /R_{int}	10108 / 0.0843	13465 / 0.0602
No. of obsd. rflns. [$I_0 > 2\sigma(I_0)$]	8707	10745
Data / restraints / parameters	10108 / 1 / 685	13465 / 0 / 685
R_1 / wR_2 [$I_0 > 2\sigma(I_0)$][a]	0.0552 / 0.1575	0.0461 / 0.0976
R_1 / wR_2 (all data)[a]	0.0658 / 0.1653	0.0664 / 0.1069
GOF (on F^2)[a]	1.010	1.034
Largest diff. peak and hole (e $Å^{-3}$)	1.525 / −1.039	1.339 / −0.816

Figure S1. ORTEP diagram of **1[BPh_4]$_2$**

Thermal ellipsoids are shown at 50% probability level. Two BPh_4^- counter anions and all hydrogen atoms on carbons are omitted for clarity.

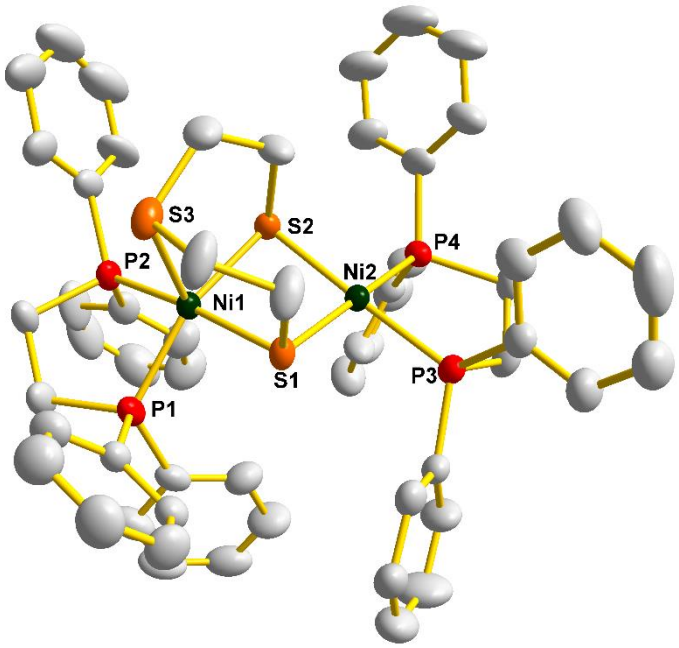

Table S3. Selected bond distances (Å) and bond angles (°) for **1[BPh_4]$_2$**

Distances (Å)			
Ni1···Ni2	3.1093(8)	Ni1–P2	2.174(2)
Ni1–S1	2.238(2)	Ni2–S1	2.217(2)
Ni1–S2	2.247(2)	Ni2–S2	2.237(2)
Ni1–S3	2.391(2)	Ni2–P3	2.178(2)
Ni1–P1	2.183(1)	Ni2–P4	2.168(2)
Angles (°)			
S1–Ni1–S2	87.86(6)	P1–Ni1–P2	83.90(6)
S1–Ni1–S3	90.28(6)	S1–Ni2–S2	88.64(5)
S2–Ni1–S3	91.79(6)	P3–Ni2–P4	86.68(6)
Torsion angles (°)			
S1–Ni1Ni2–S2	151.45(8)	Ni1S1S2/Ni1P1P2	25.55(6)
Ni2S1S2/Ni2P3P4	3.65(6)	Ni1S1S2/Ni2S1S2	28.57(5)

Figure S2. ORTEP diagram of **2[PF_6]$_2$**·2CH_2Cl_2

Thermal ellipsoids are shown at 50% probability level. Two PF_6^- counter anions, the two co-crystallized CH_2Cl_2 molecules and all hydrogen atoms on carbons are omitted for clarity.

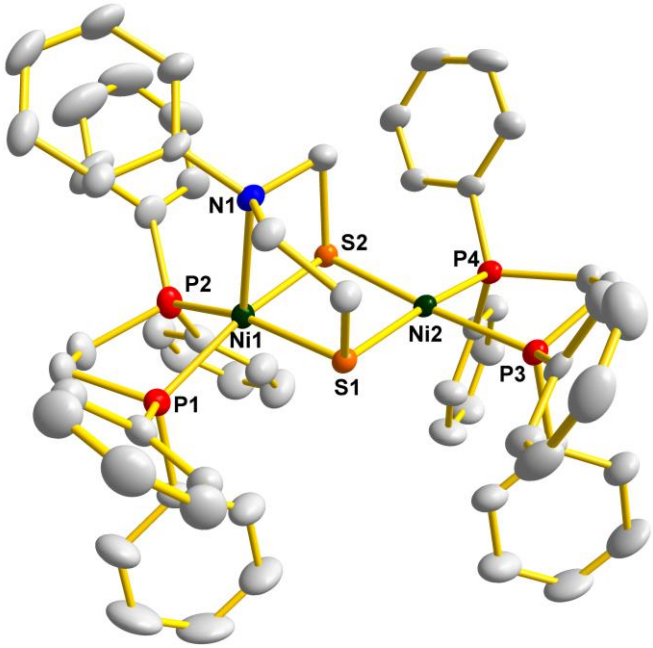

Table S4. Selected bond distances (Å) and bond angles (°) for **2[PF_6]$_2$**·2CH_2Cl_2

Distances (Å)			
Ni1···Ni2	3.2048(6)	Ni1–P2	2.1731(10)
Ni1–S1	2.2574(9)	Ni2–S1	2.2378(9)
Ni1–S2	2.2185(9)	Ni2–S2	2.2283(8)
Ni1–N1	2.475(3)	Ni2–P3	2.1754(9)
Ni1–P1	2.1757(10)	Ni2–P4	2.1872(10)
Angles (°)			
S1–Ni1–S2	87.86(3)	P1–Ni1–P2	85.51(4)
S1–Ni1–N1	80.84(7)	S1–Ni2–S2	88.11(3)
S2–Ni1–N1	84.97(7)	P3–Ni2–P4	85.57(4)
Torsion angles (°)			
S1–Ni1Ni2–S2	169.98(4)	Ni1S1S2/Ni1P1P2	21.52(3)
Ni2S1S2/Ni2P3P4	8.45(4)	Ni1S1S2/Ni2S1S2	9.71(3)

Figure S3. ORTEP diagram of **3[PF$_6$]**·MeCN

Thermal ellipsoids are shown at 50% probability level. One PF_6^- counter anion, one co-crystallized MeCN molecule and all hydrogen atoms on carbons are omitted for clarity.

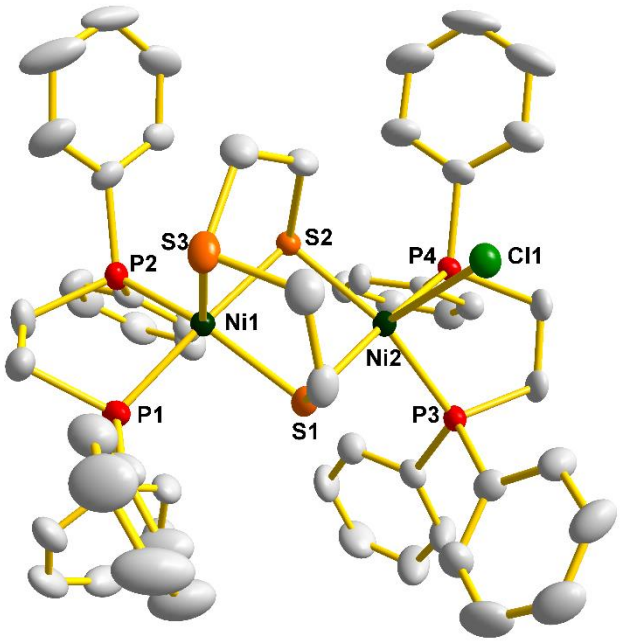

Table S5. Selected bond distances (Å) and bond angles (˚) for **3[PF$_6$]**·MeCN

Distances (Å)			
Ni1···Ni2	3.2528(10)	Ni2–S1	2.239(2)
Ni1–S1	2.250(1)	Ni2–S2	2.244(1)
Ni1–S2	2.242(1)	Ni2–P3	2.170(1)
Ni1–S3	2.392(2)	Ni2–P4	2.188(2)
Ni1–P1	2.158(2)	Ni2–Cl1	2.614(2)
Ni1–P2	2.180(2)		
Angles (°)			
S1–Ni1–S2	86.55(5)	S1–Ni2–S2	86.77(5)
S1–Ni1–S3	91.87(6)	S1–Ni2–Cl1	104.38(5)
S2–Ni1–S3	90.05(5)	S2–Ni2–Cl1	105.62(5)
P1–Ni1–P2	84.80(6)	P3–Ni2–P4	84.63(5)
Torsion angles (°)			
S1–Ni1Ni2–S2	169.76(7)	Ni1S1S2/Ni1P1P2	22.07(6)
Ni2S1S2/Ni2P3P4	21.54(4)	Ni1S1S2/Ni2S1S2	9.70(4)

Figure S4. ORTEP diagram of **4[PF$_6$]**·CH_2Cl_2

Thermal ellipsoids are shown at 50% probability level. One PF_6^- counter anion, one co-crystallized CH_2Cl_2 molecule and all hydrogen atoms on carbons are omitted for clarity.

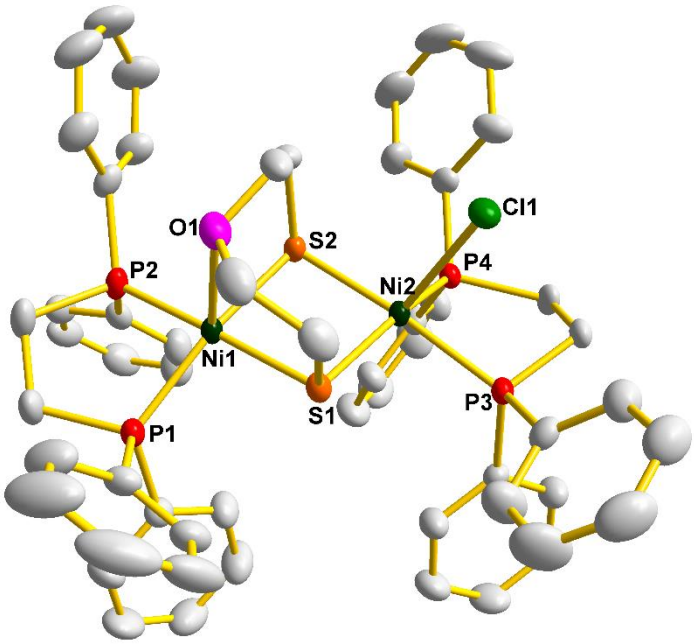

Table S6. Selected bond distances (Å) and bond angles (°) for **4[PF$_6$]**·CH_2Cl_2

Distances (Å)			
Ni1···Ni2	3.2276(4)	Ni2–S1	2.2533(8)
Ni1–S1	2.2462(7)	Ni2–S2	2.2390(7)
Ni1–S2	2.2365(8)	Ni2–P3	2.1934(7)
Ni1–O1	2.377(2)	Ni2-P4	2.1750(8)
Ni1–P1	2.1790(8)	Ni2-Cl1	2.5955(8)
Ni1–P2	2.1701(8)		
Angles (°)			
S1–Ni1–S2	87.34(3)	S1–Ni2–S2	87.10(3)
S1–Ni1–O1	83.20(5)	S1–Ni2–Cl1	105.14(3)
S2–Ni1–O1	82.49(6)	S2–Ni2–Cl1	105.34(3)
P1–Ni1–P2	85.44(3)	P3–Ni2–P4	84.96(3)
Torsion angles (°)			
S1–Ni1Ni2–S2	166.26(4)	Ni1S1S2/Ni1P1P2	15.26(2)
Ni2S1S2/Ni2P3P4	21.65(2)	Ni1S1S2/Ni2S1S2	13.18(1)

ESI-HRMS

Figure S5. ESI-HRMS of **1[PF$_6$]$_2$** in MeCN

(a) The signal at an *m/z* = 532.0626 corresponds to [**1**]$^{2+}$. (b) Calculated isotopic distribution for [**1**]$^{2+}$ (upper) and the amplifying experimental diagram for [**1**]$^{2+}$ (bottom).

(a)

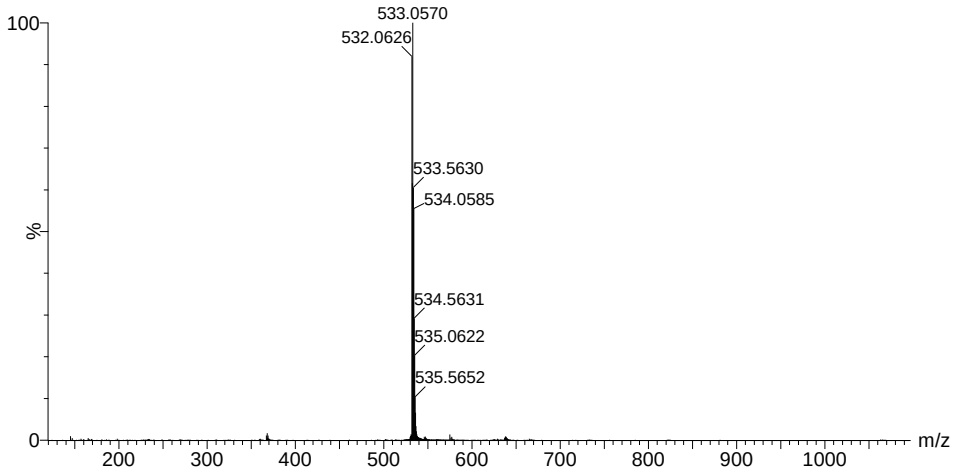

(b)

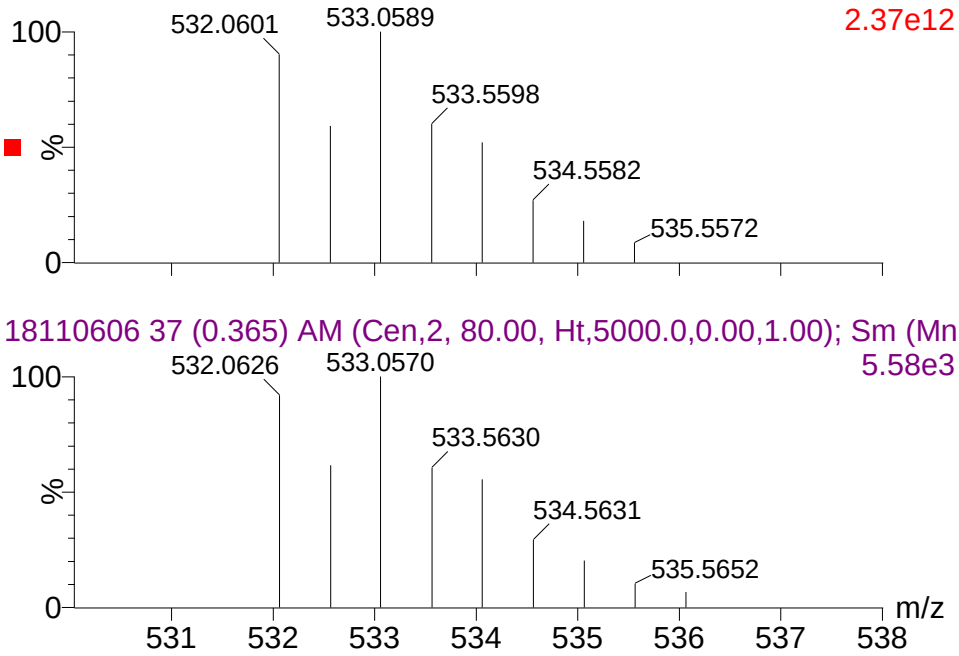

Figure S6. ESI-HRMS of **1[BPh$_4$]$_2$** in MeCN

(a) The signal at an *m/z* = 532.0604 corresponds to [**1**]$^{2+}$. (b) Calculated isotopic distribution for [**1**]$^{2+}$ (upper) and the amplifying experimental diagram for [**1**]$^{2+}$ (bottom).

(a)

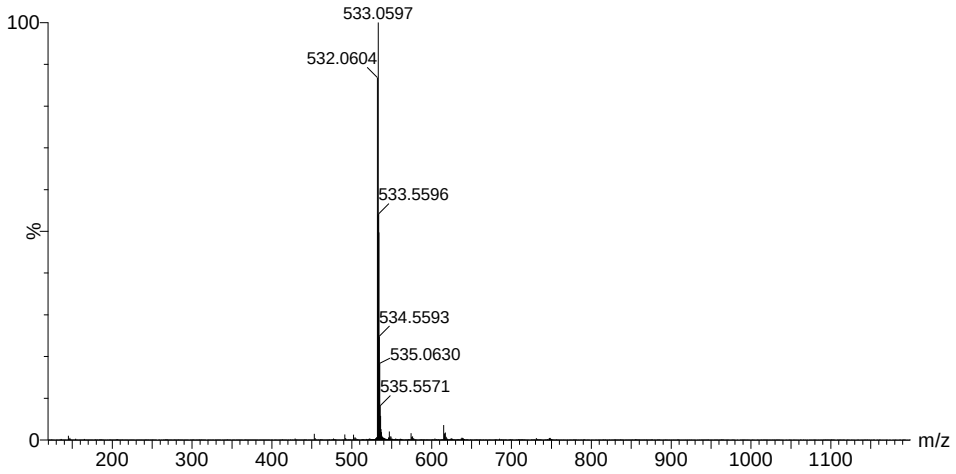

(b)

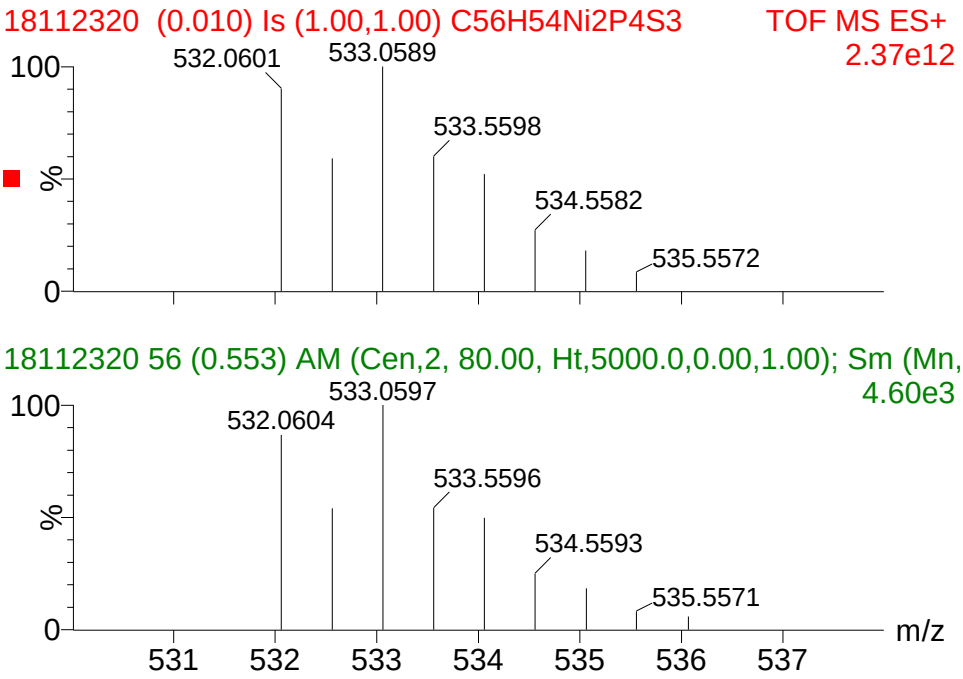

Figure S7. ESI-HRMS of **2[PF$_6$]$_2$** in MeCN

(a) The signal at an *m/z* = 561.5931 corresponds to [**2**]$^{2+}$. (b) Calculated isotopic distribution for [**2**]$^{2+}$ (upper) and the amplifying experimental diagram for [**2**]$^{2+}$ (bottom).

(a)

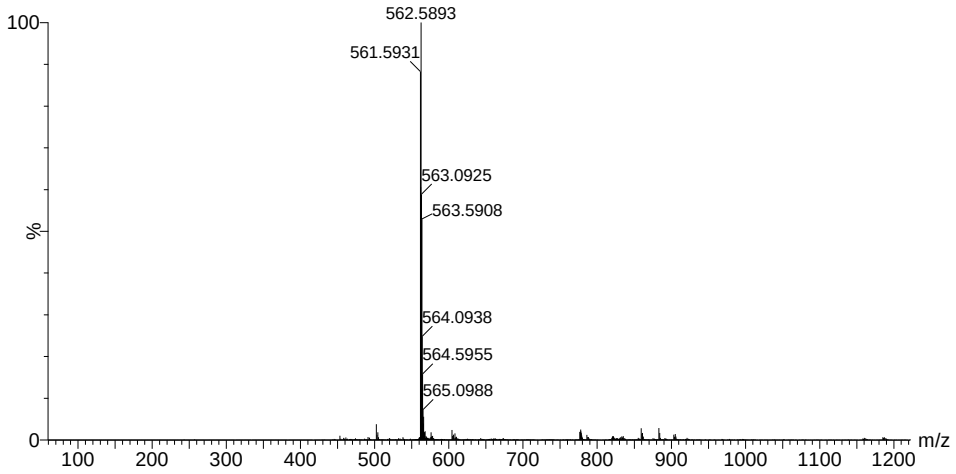

(b)

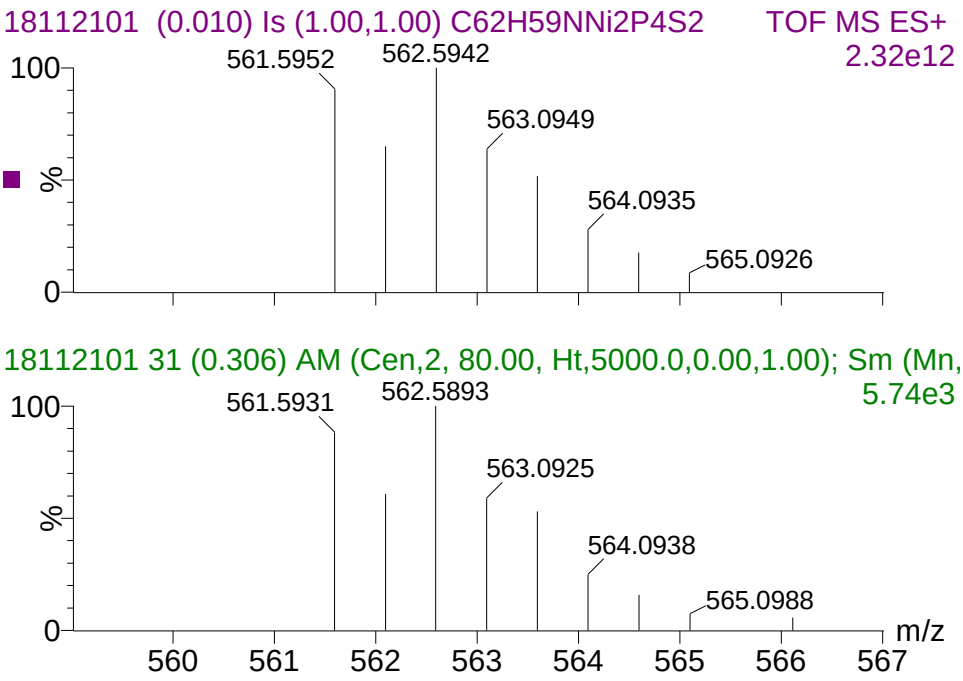

Figure S8. ESI-HRMS of **3[PF$_6$]** in MeCN

(a) The signal at an *m/z* = 1099.0873 corresponds to [**3**]$^+$. (b) Calculated isotopic distribution for [**3**]$^+$ (upper) and the amplifying experimental diagram for [**3**]$^+$ (bottom).

(a)

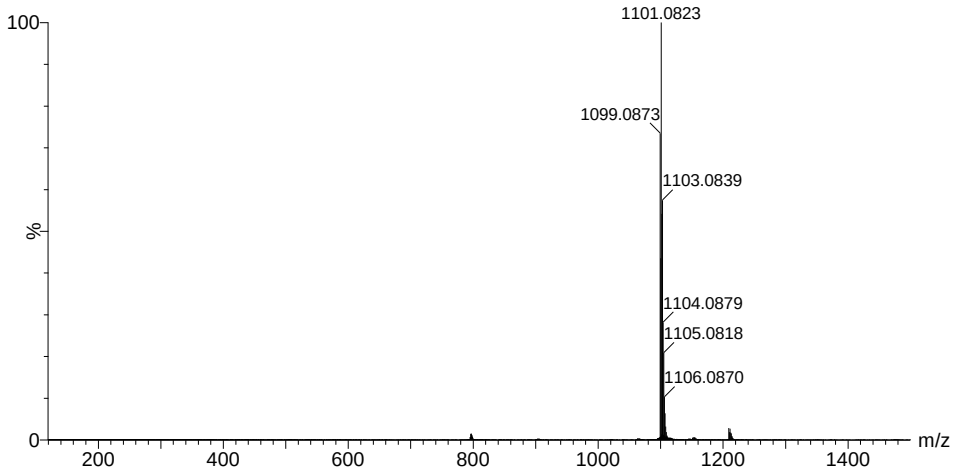

(b)

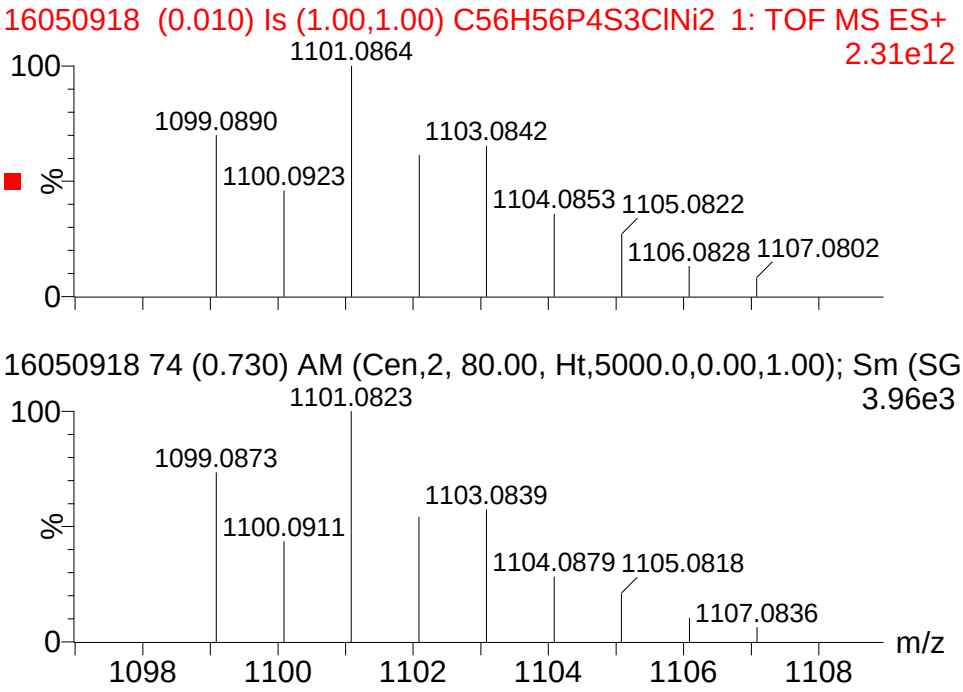

Figure S9. ESI-HRMS of **4[PF$_6$]** in MeCN

(a) The signal at an *m/z* = 1083.1136 corresponds to [**4**]$^+$. (b) Calculated isotopic distribution for [**4**]$^+$ (upper) and the amplifying experimental diagram for [**4**]$^+$ (bottom).

(a)

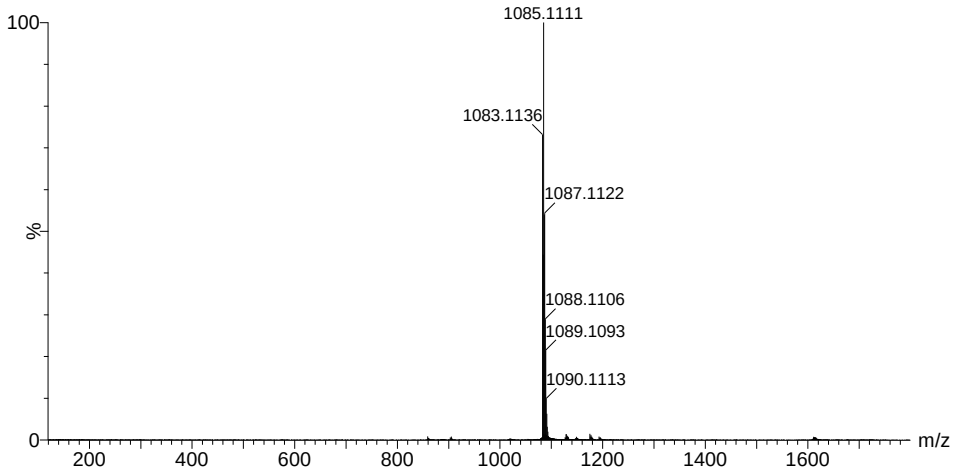

(b)

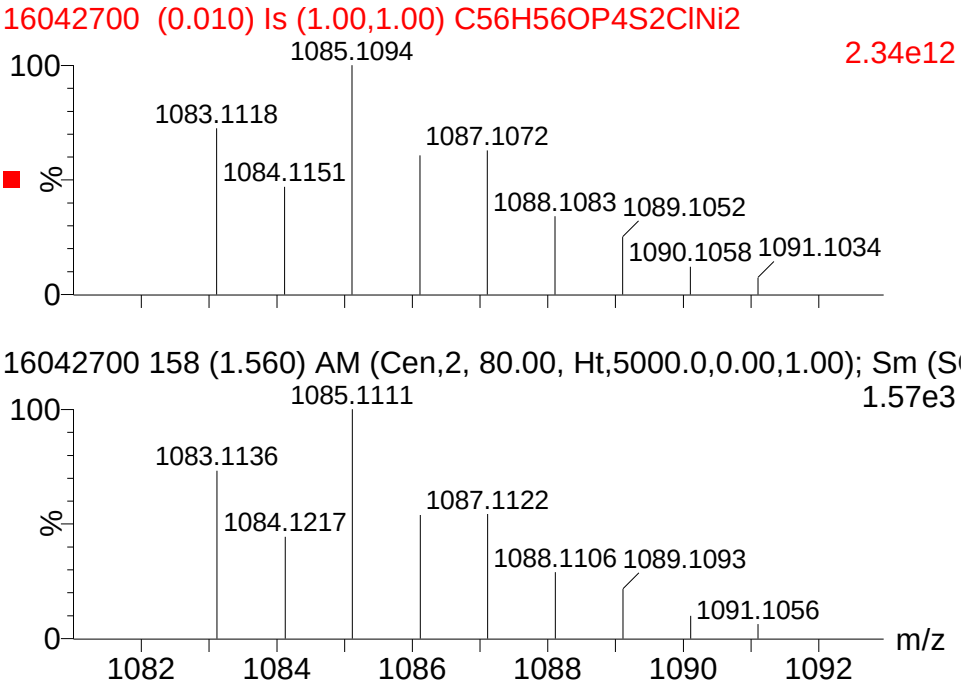

NMR spectra

Figure S10. The ^{1}H NMR spectrum of **1[PF$_6$]$_2$** in CD_2Cl_2

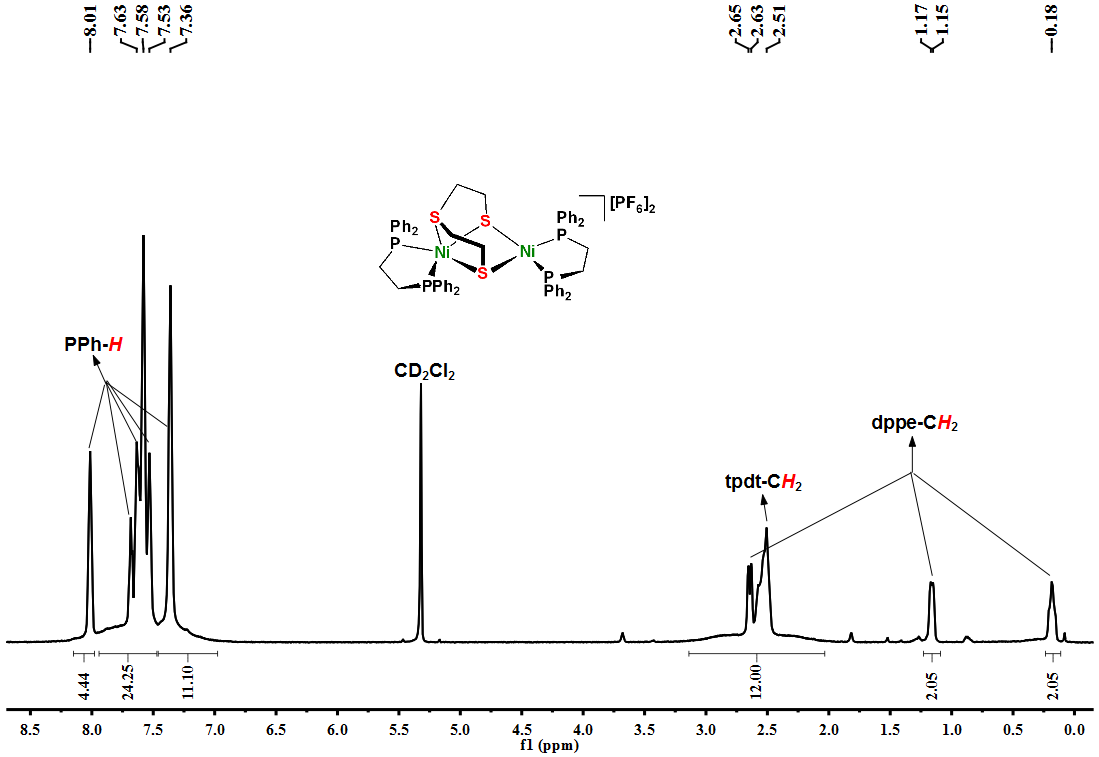

Figure S11. The ^{1}H, ^{1}H-COSY spectrum of **1[PF$_6$]$_2$** in CD_2Cl_2

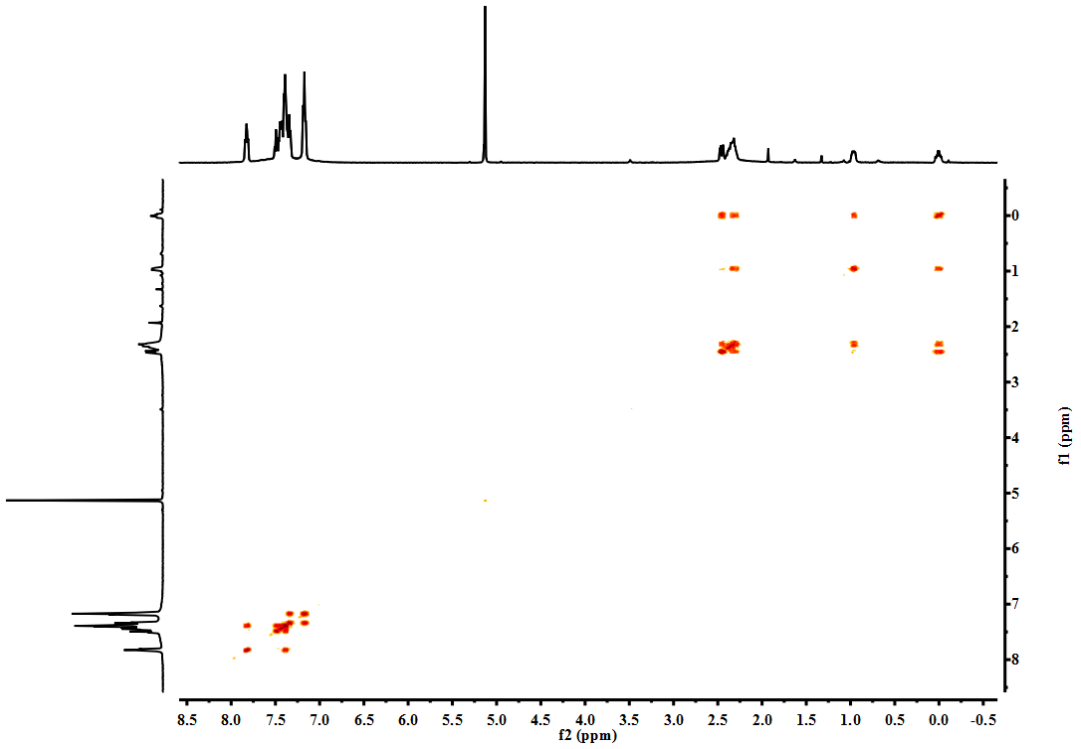

Figure S12. The $^{13}C\{^{1}H\}$ NMR spectrum of **1[PF$_6$]$_2$** in CD_2Cl_2

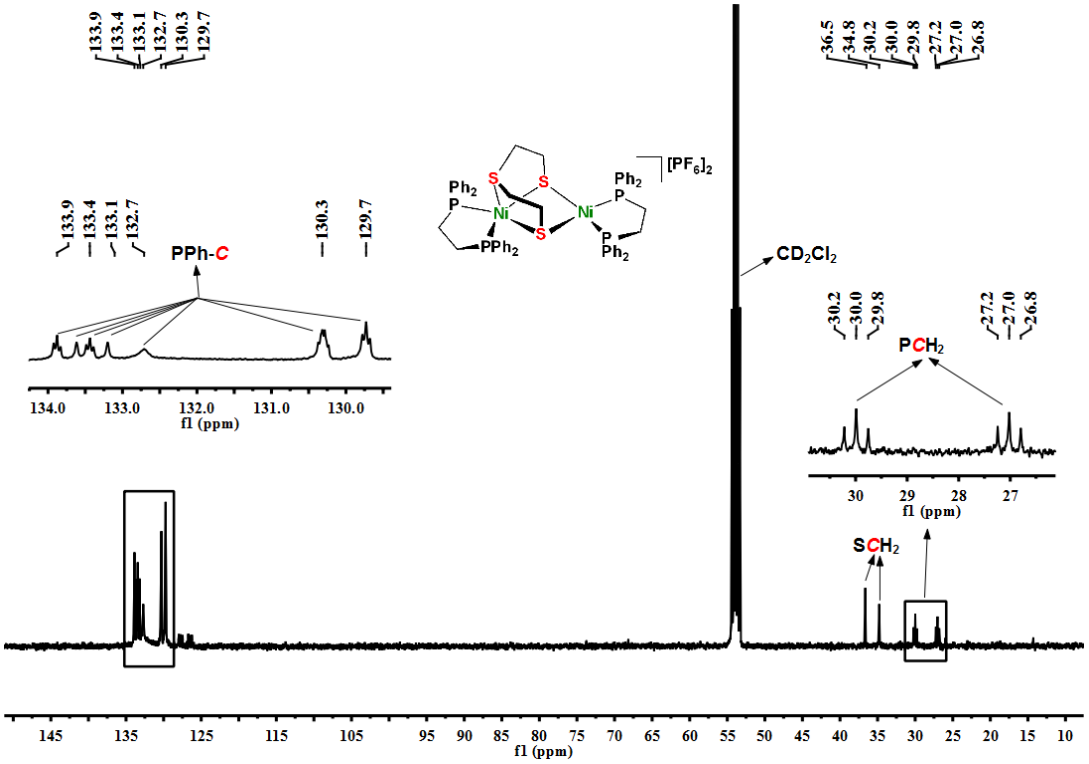

Figure S13. The $^{31}P\{^{1}H\}$ NMR spectrum of **1[PF$_6$]$_2$** in CD_2Cl_2

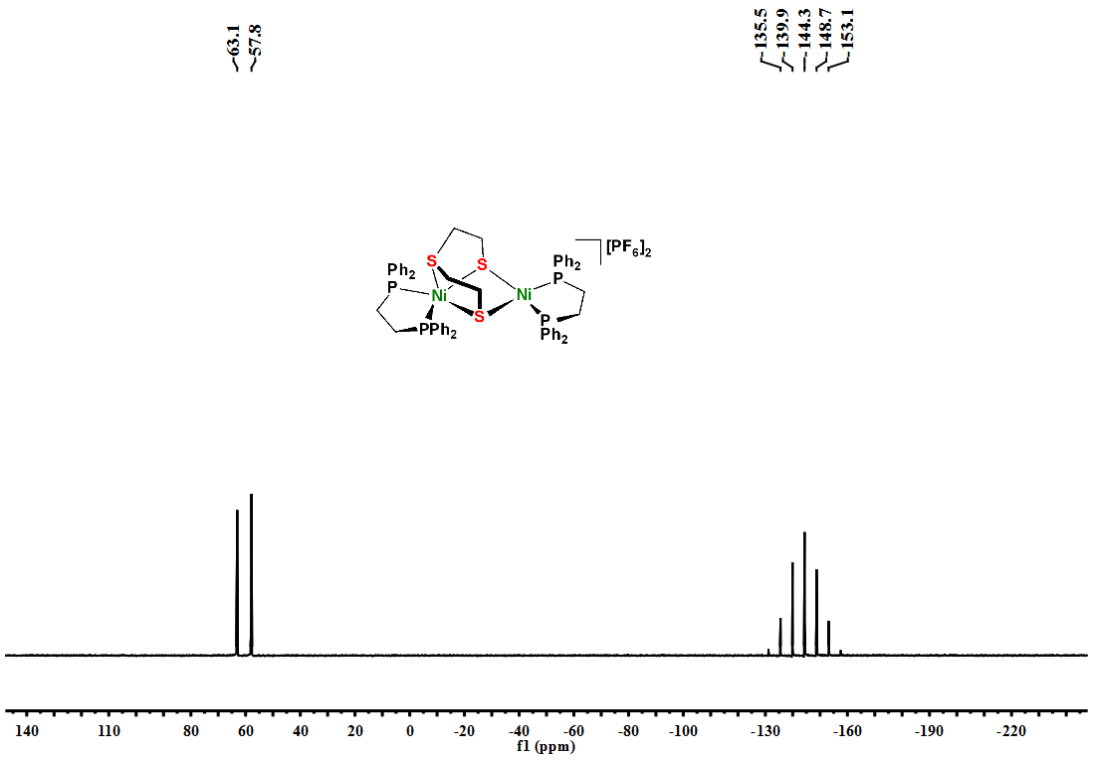

Figure S14. The ^{1}H NMR spectrum of **1[BPh$_4$]$_2$** in CD_2Cl_2

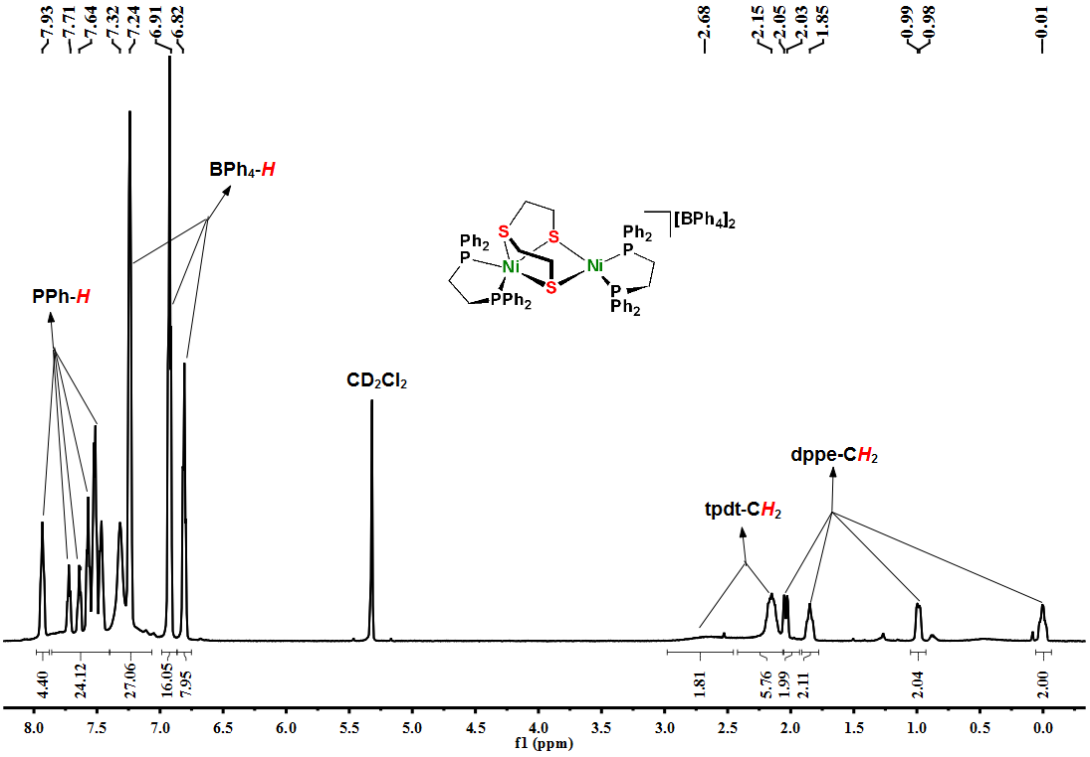

Figure S15. The ^{13}C{^{1}H} NMR spectrum of **1[BPh$_4$]$_2$** in CD_2Cl_2

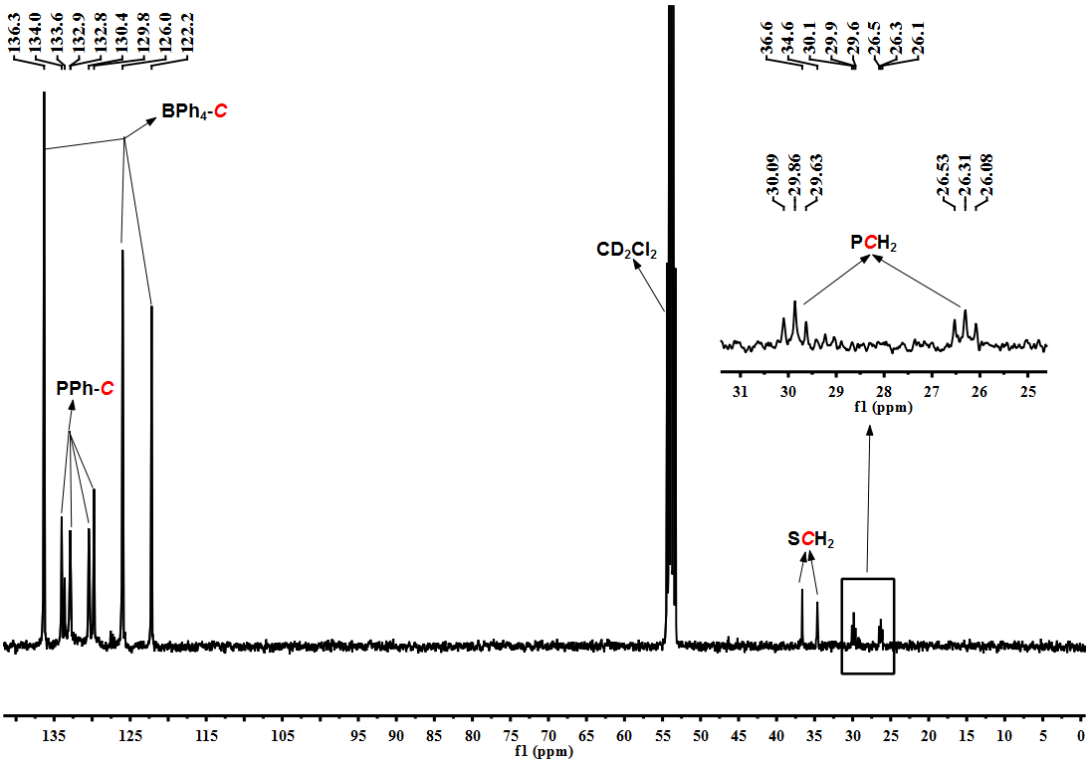

Figure S16. The $^{31}P\{^{1}H\}$ NMR spectrum of **1[BPh$_4$]$_2$** in CD_2Cl_2

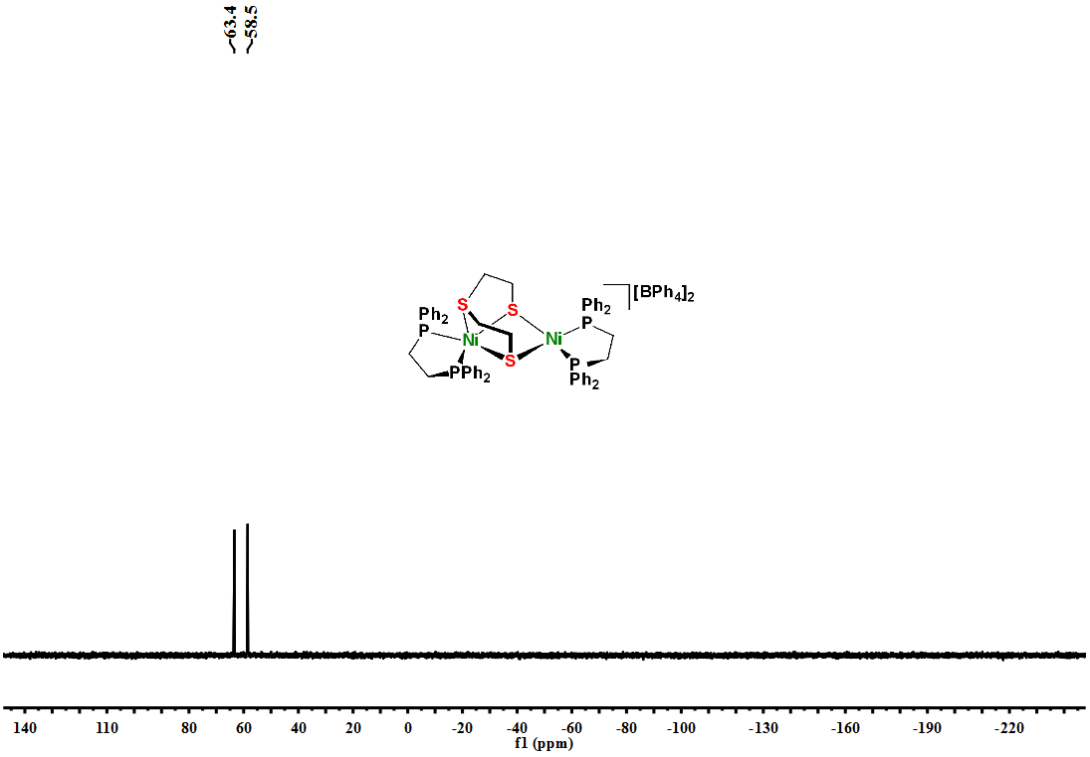

Figure S17. The ^{1}H NMR spectrum of **2[PF$_6$]$_2$** in CD_2Cl_2

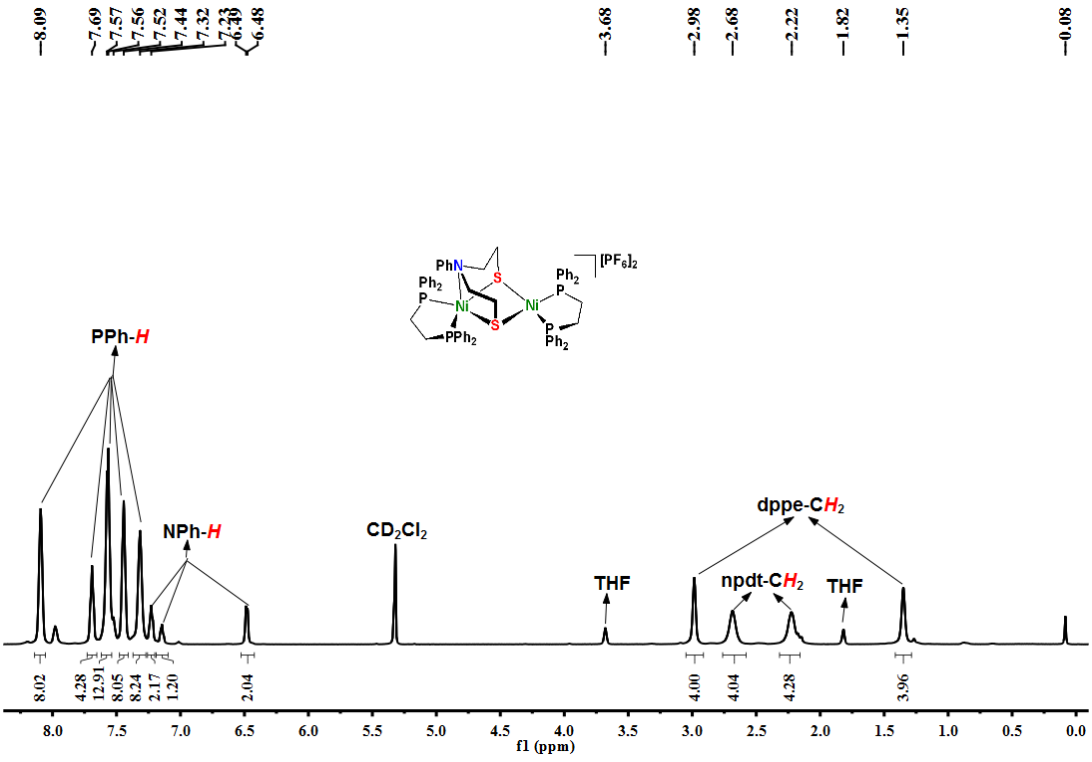

Figure S18. The $^{13}C\{^{1}H\}$ NMR spectrum of **2[PF$_6$]$_2$** in CD_2Cl_2

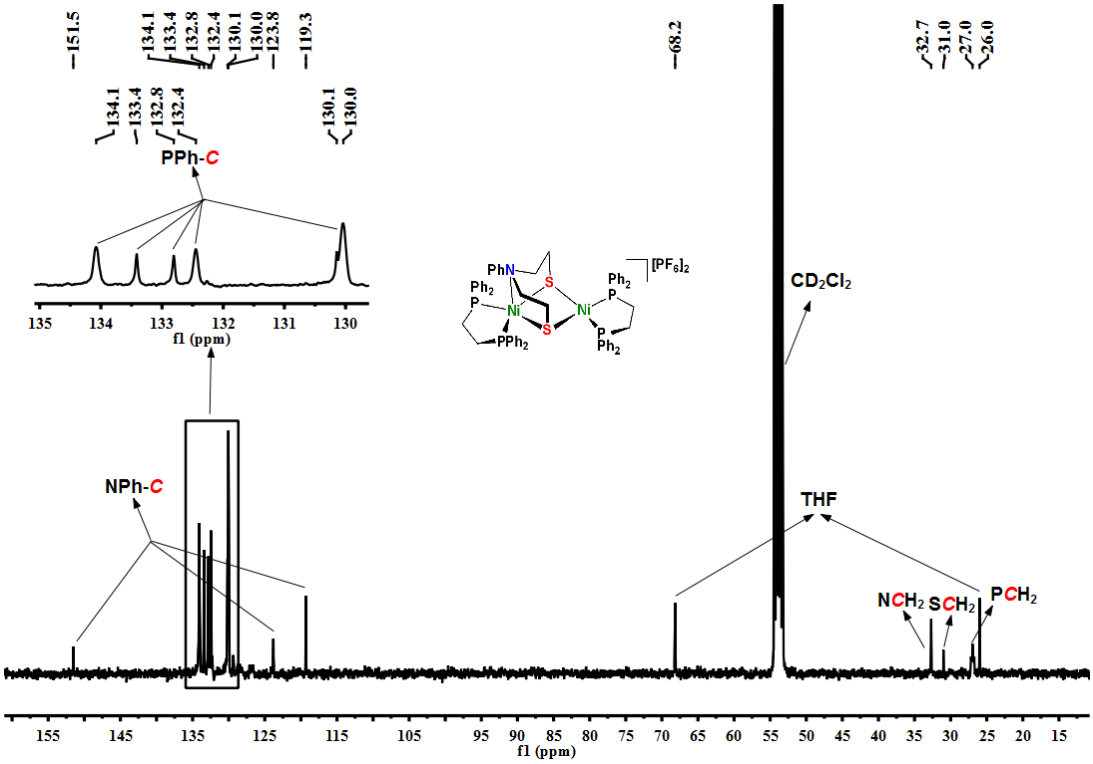

Figure S19. The $^{31}P\{^{1}H\}$ NMR spectrum of **2[PF$_6$]$_2$** in CD_2Cl_2

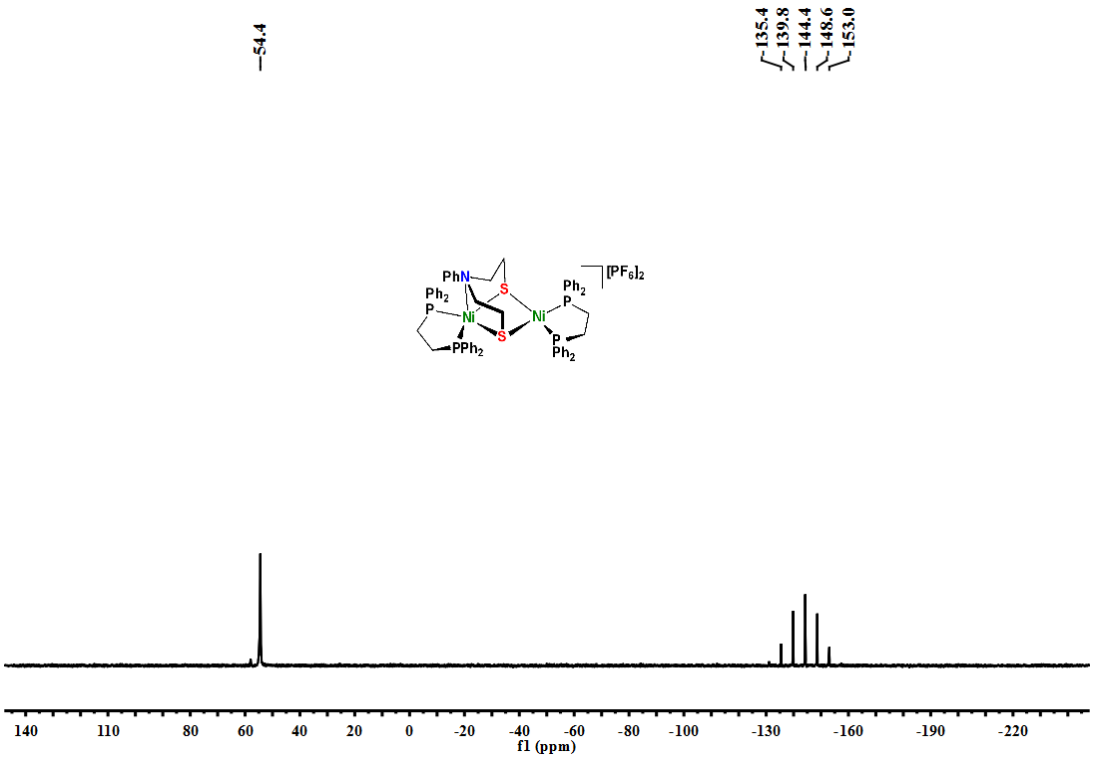

Figure S20. The ^{1}H NMR spectrum of **3[PF$_6$]** in CD_2Cl_2

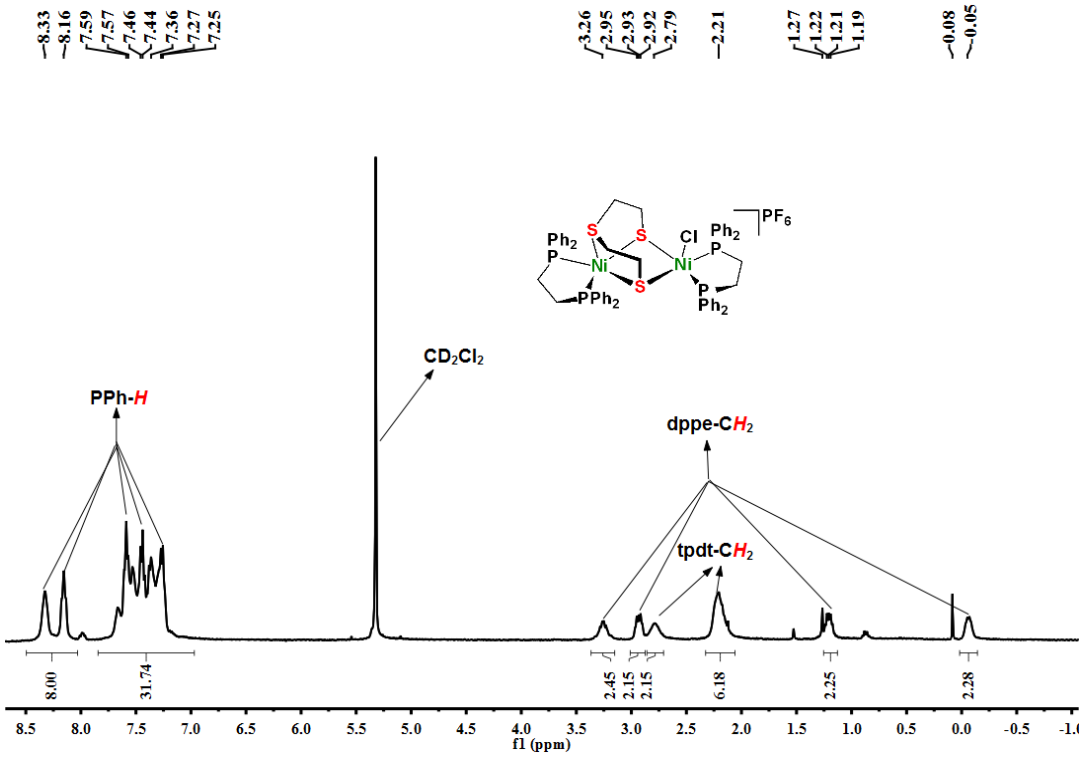

Figure S21. The $^{13}C\{^{1}H\}$ NMR spectrum of **3[PF$_6$]** in CD_2Cl_2

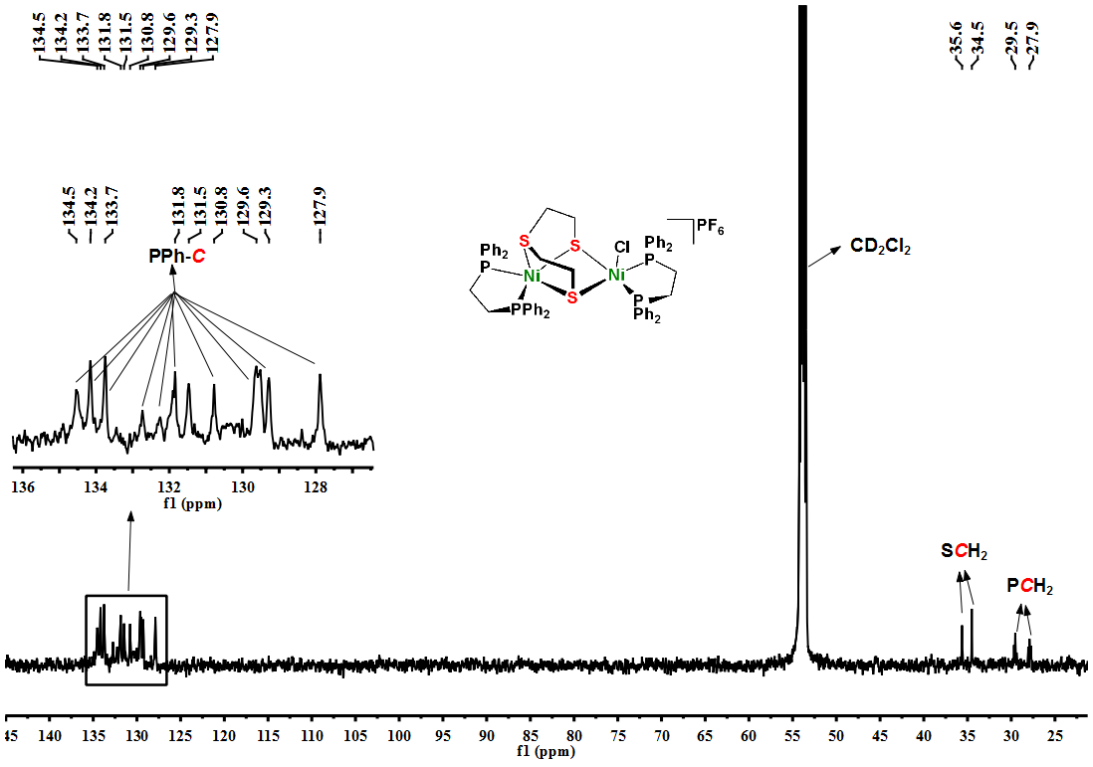

Figure S22. The $^{31}P\{^{1}H\}$ NMR spectrum of **3[PF_6]** in CD_2Cl_2

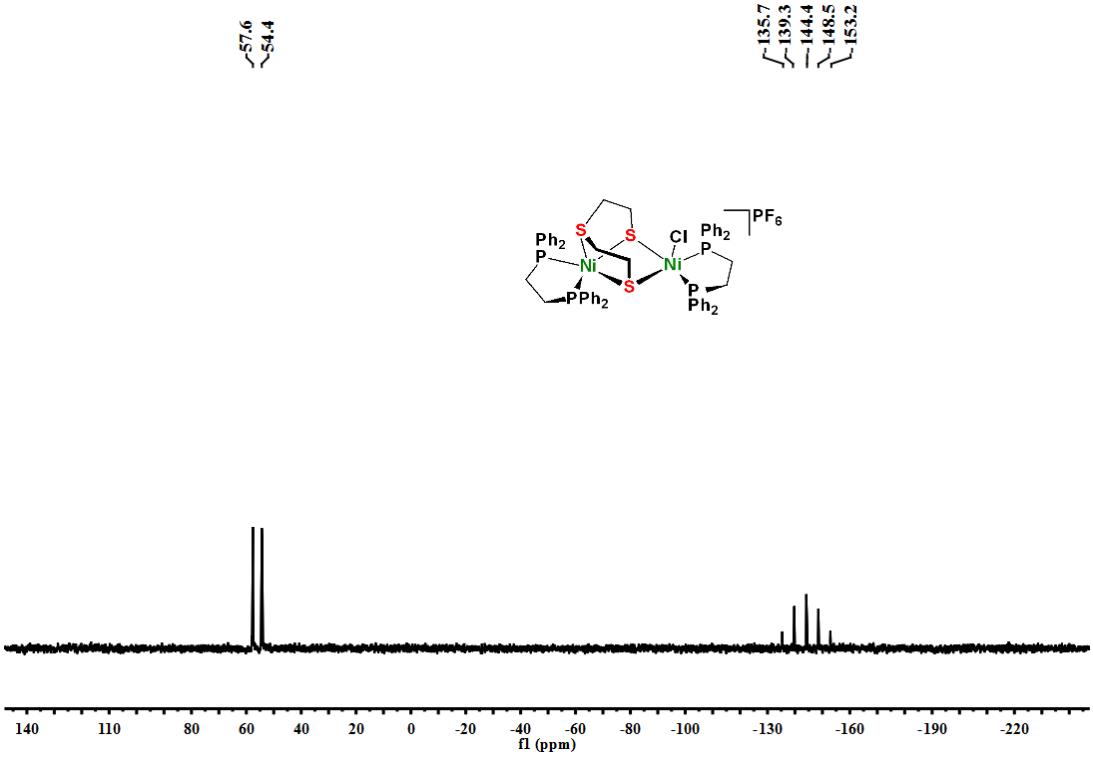

Figure S23. The ^{1}H NMR spectrum of **4[PF_6]** in CD_2Cl_2

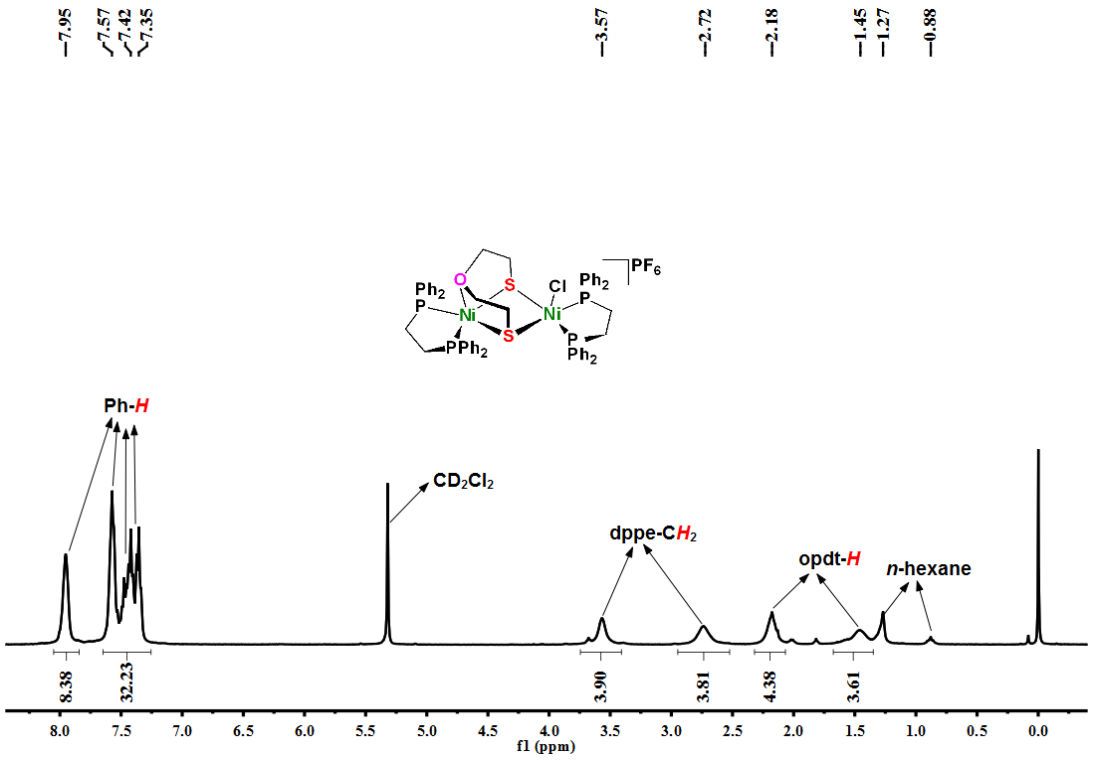

Figure S24. The $^{13}C\{^{1}H\}$ NMR spectrum of **4[PF$_6$]** in CD_2Cl_2

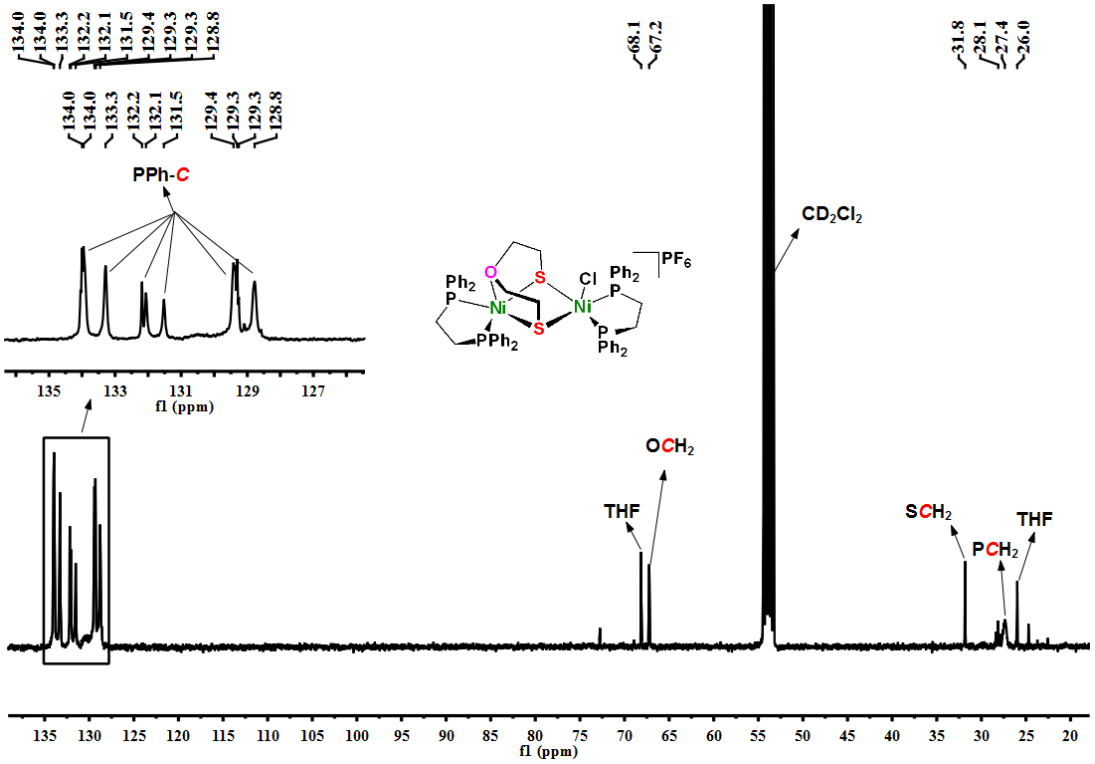

Figure S25. The $^{31}P\{^{1}H\}$ NMR spectrum of **4[PF$_6$]** in CD_2Cl_2

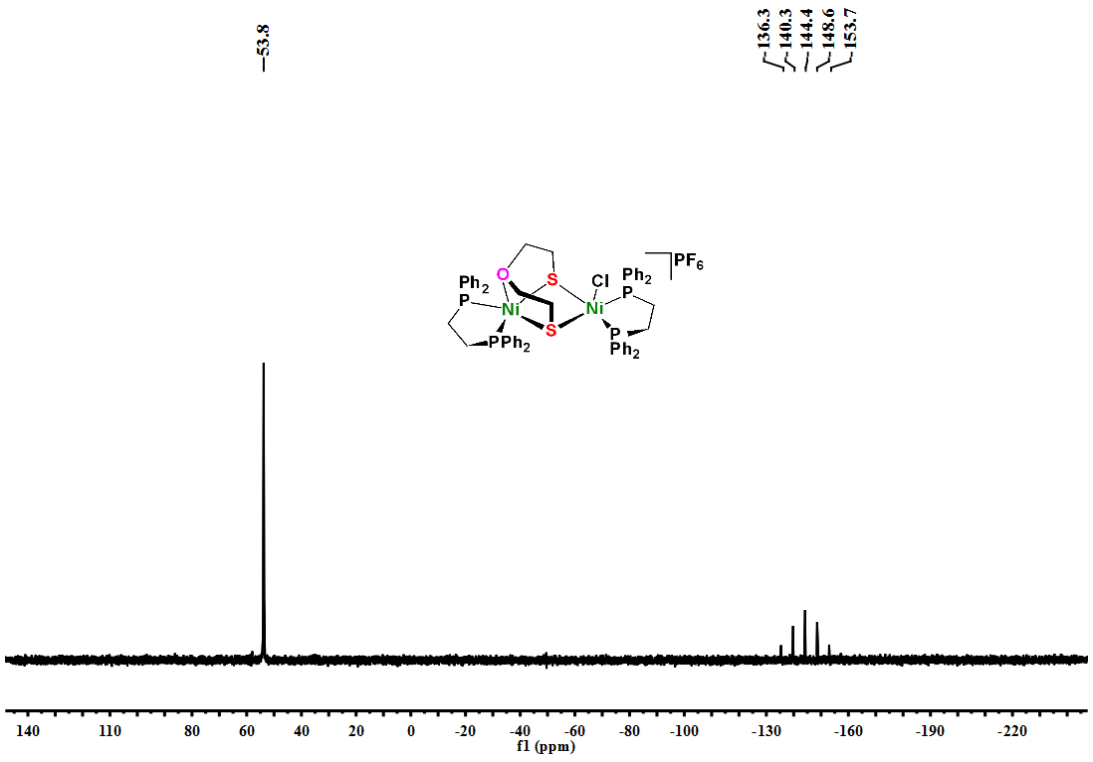

IR spectra

Figure S26. The IR (film) spectrum of **1[PF_6]$_2$**

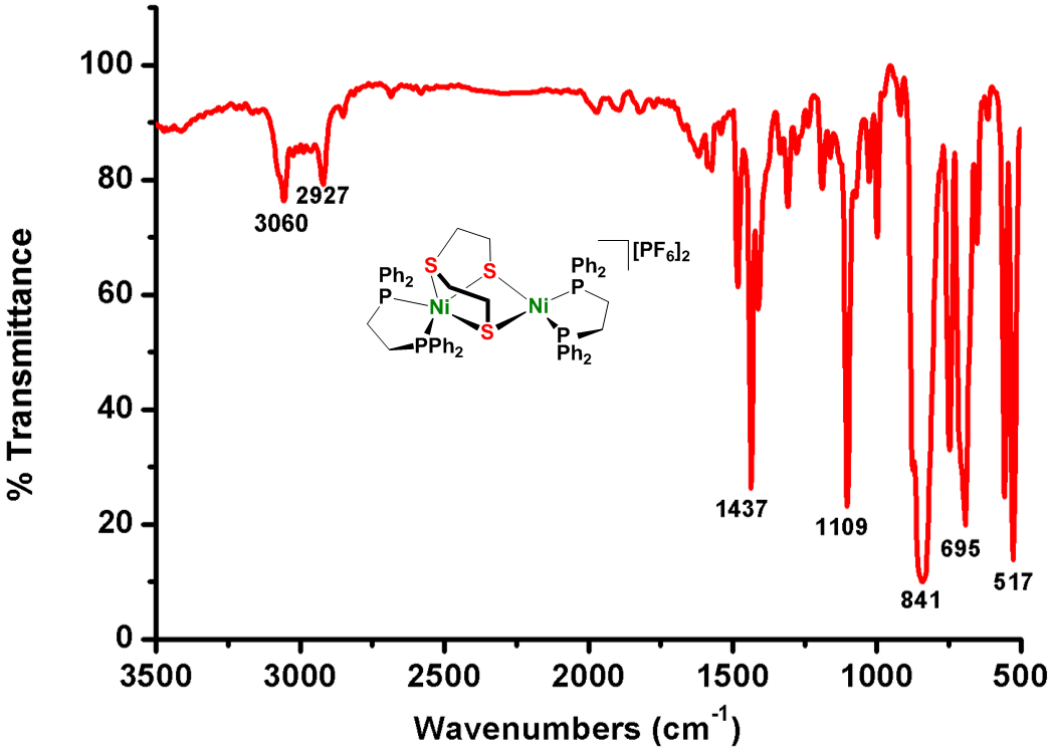

Figure S27. The IR (film) spectrum of **1[BPh_4]$_2$**

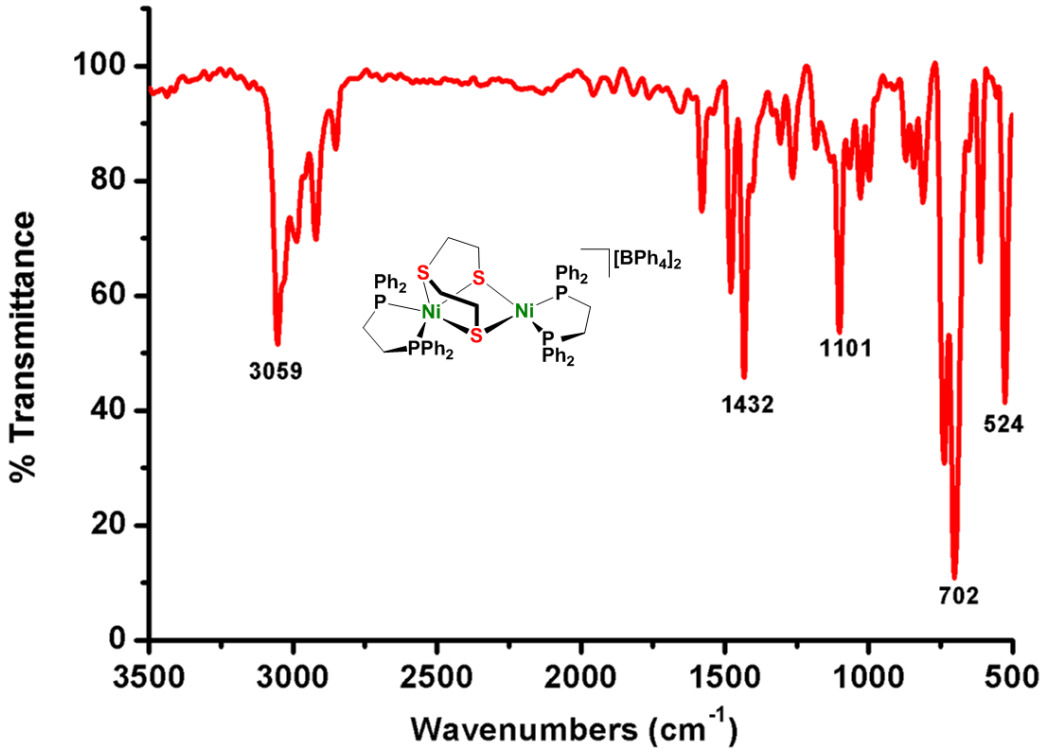

Figure S28. The IR (film) spectrum of **2[PF$_6$]$_2$**

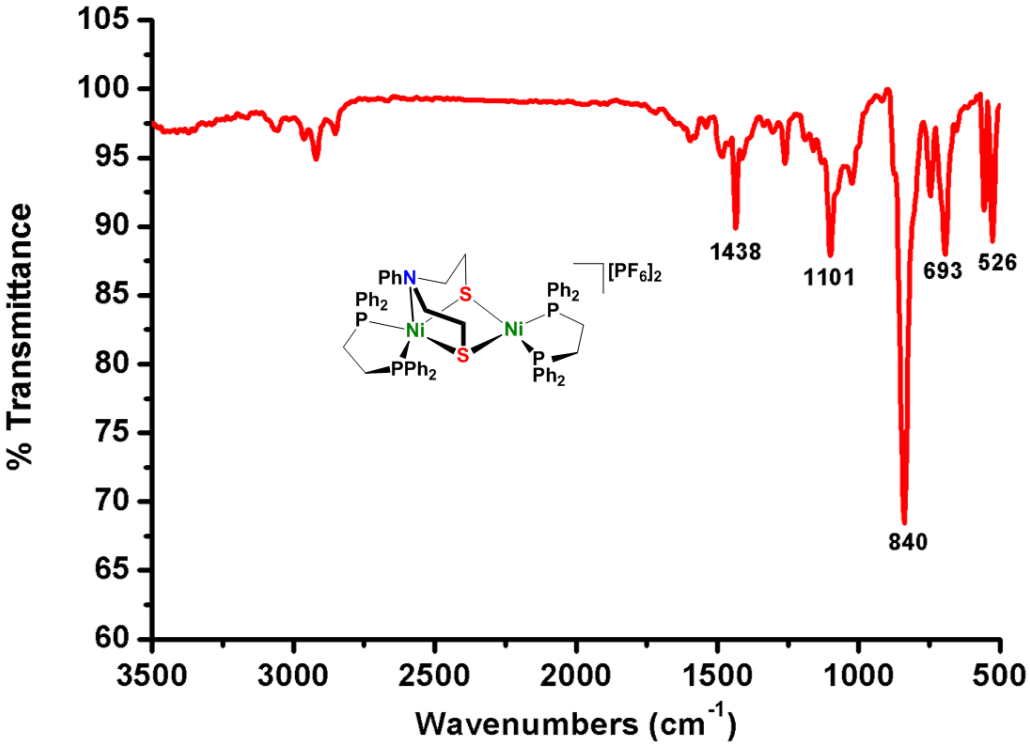

Figure S29. The IR (film) spectrum of **3[PF$_6$]**

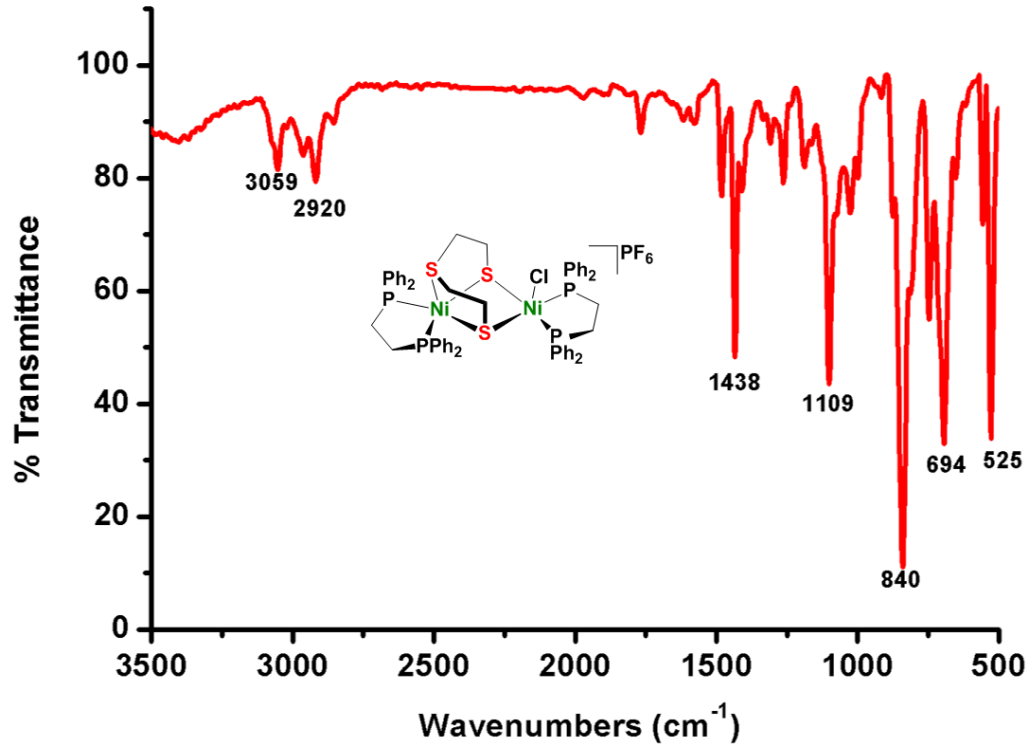

Figure S30. The IR (film) spectrum of **4[PF$_6$]**

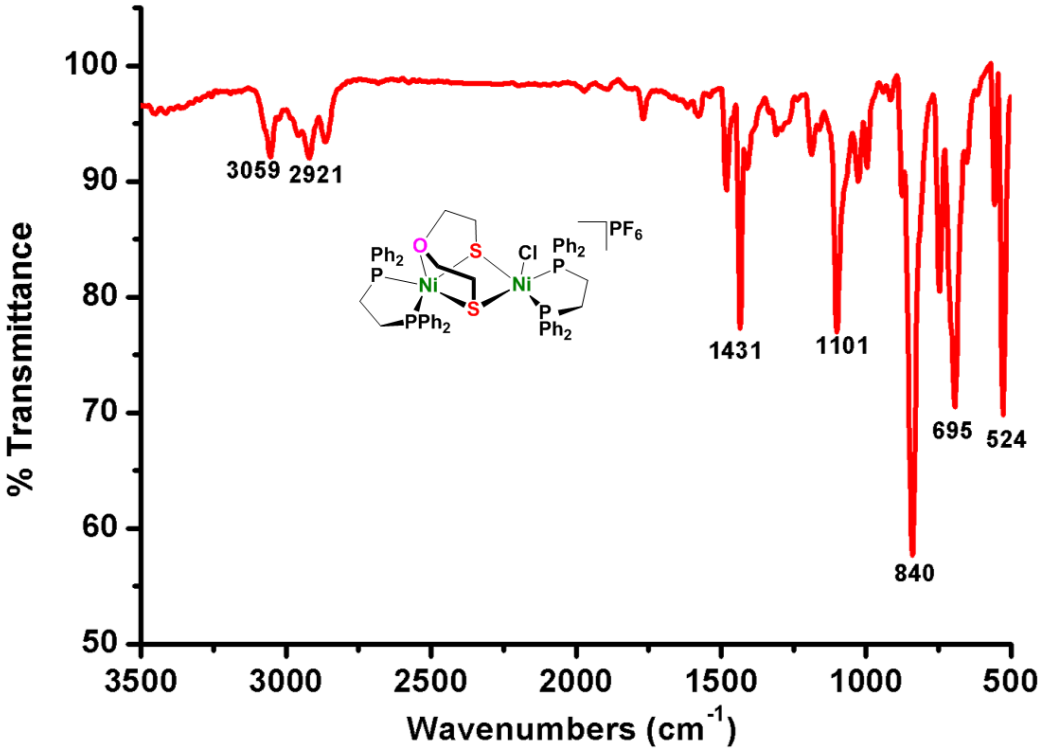

Electrochemistry

Figure S31. The cyclic voltammogram of **1[PF$_6$]$_2$** (1 mM) in 0.1 M ^{n}Bu$_4$NPF$_6$/MeCN at 25 °C with a scan rate of 100 mV s^{-1}

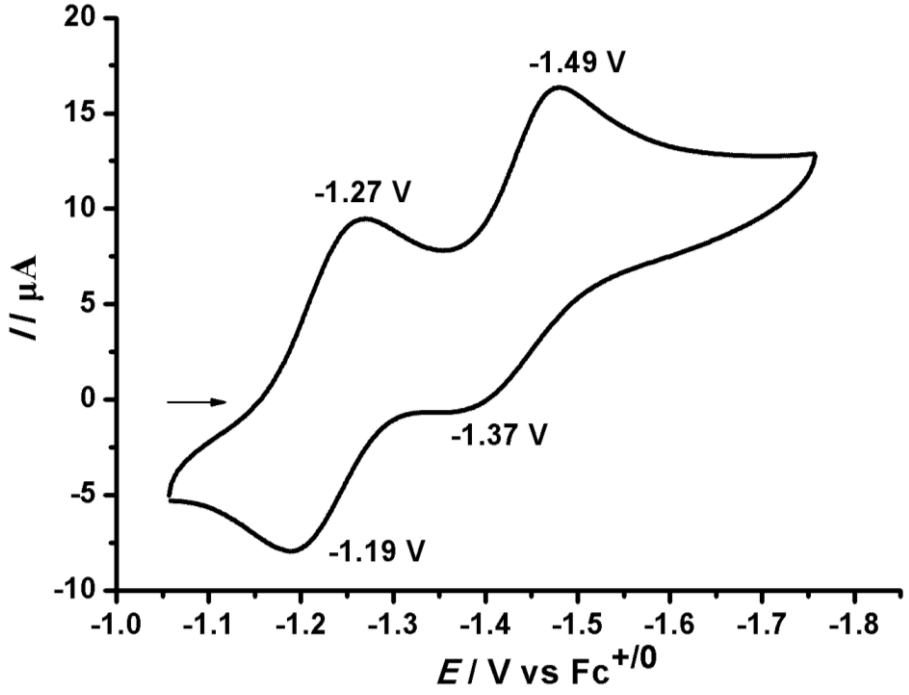

Figure S32. The cyclic voltammogram of **1[PF$_6$]$_2$** (1 mM) in 0.1 M ^{n}Bu$_4$NPF$_6$/CH$_2$Cl$_2$ at 25 °C with a scan rate of 100 mV s^{-1}

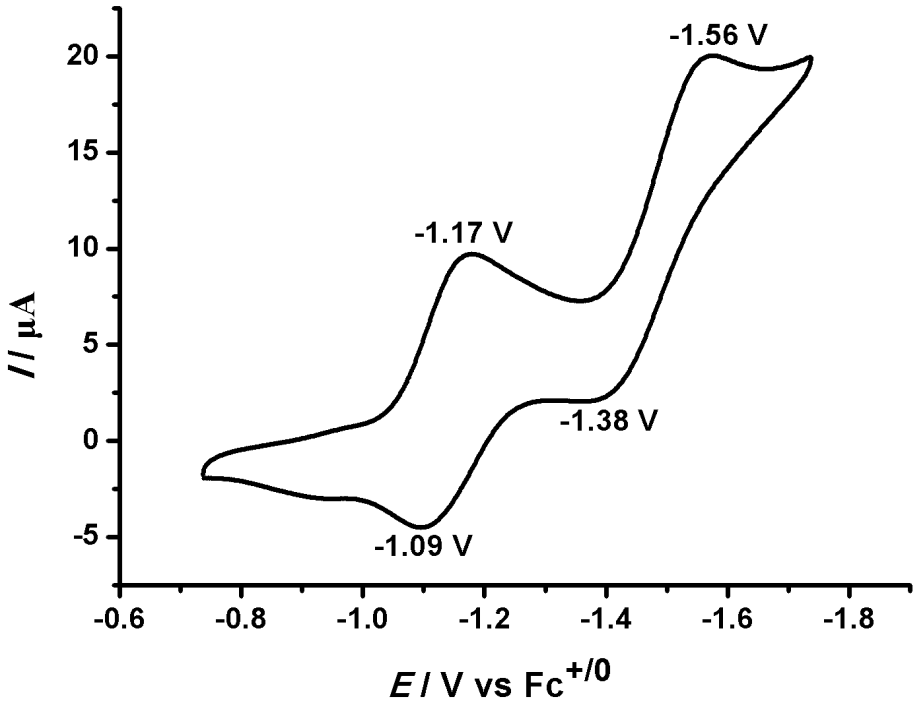

Figure S33. The cyclic voltammograms of **1[PF$_6$]$_2$** (1 mM) in 0.1 M ^{n}Bu$_4$NPF$_6$/MeCN at 25 °C at different scan rates (0.1~0.7 V s^{-1})

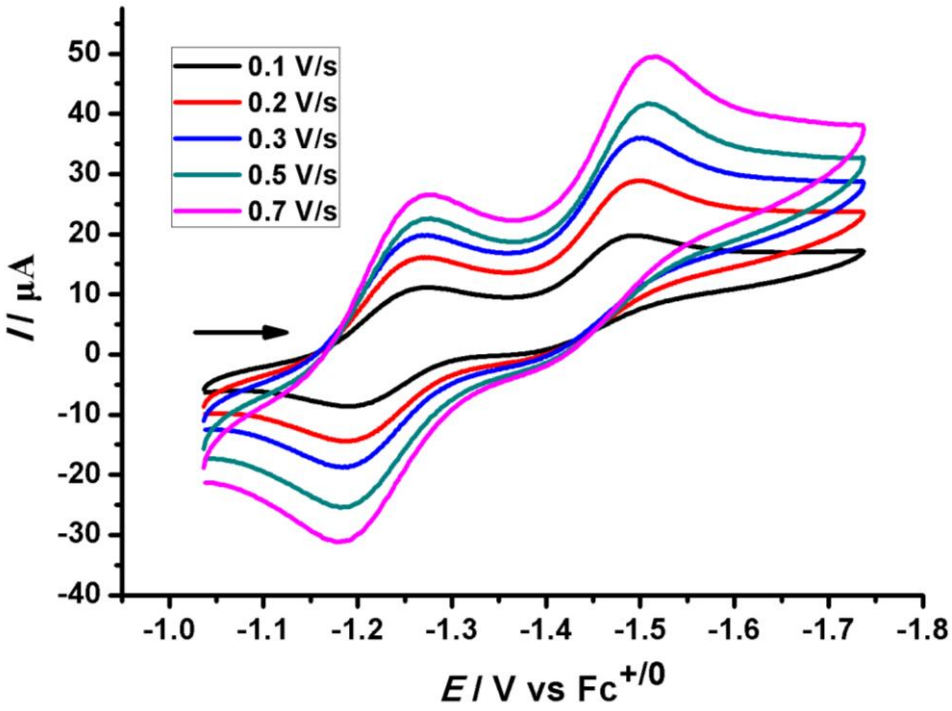

Figure S34. Plot of i_p versus $v^{1/2}$ for the second reduction peak of **1[PF$_6$]$_2$**

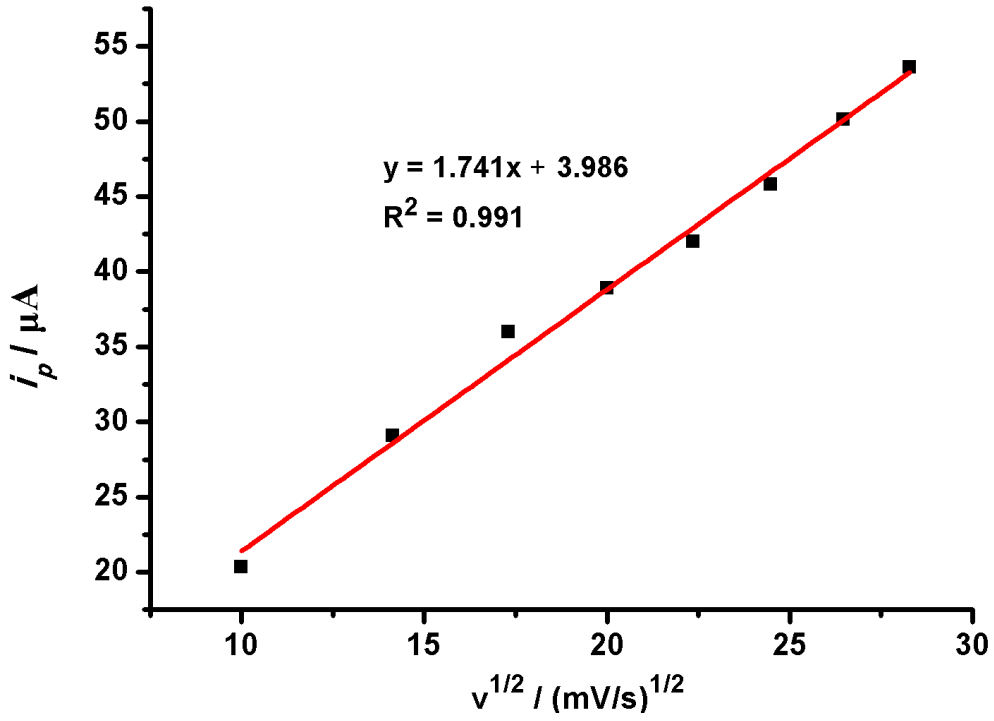

Figure S35. The cyclic voltammogram of **2[PF$_6$]$_2$** (1 mM) in 0.1 M ^{n}Bu$_4$NPF$_6$/MeCN at 25 °C with a scan rate of 100 mV s^{-1}

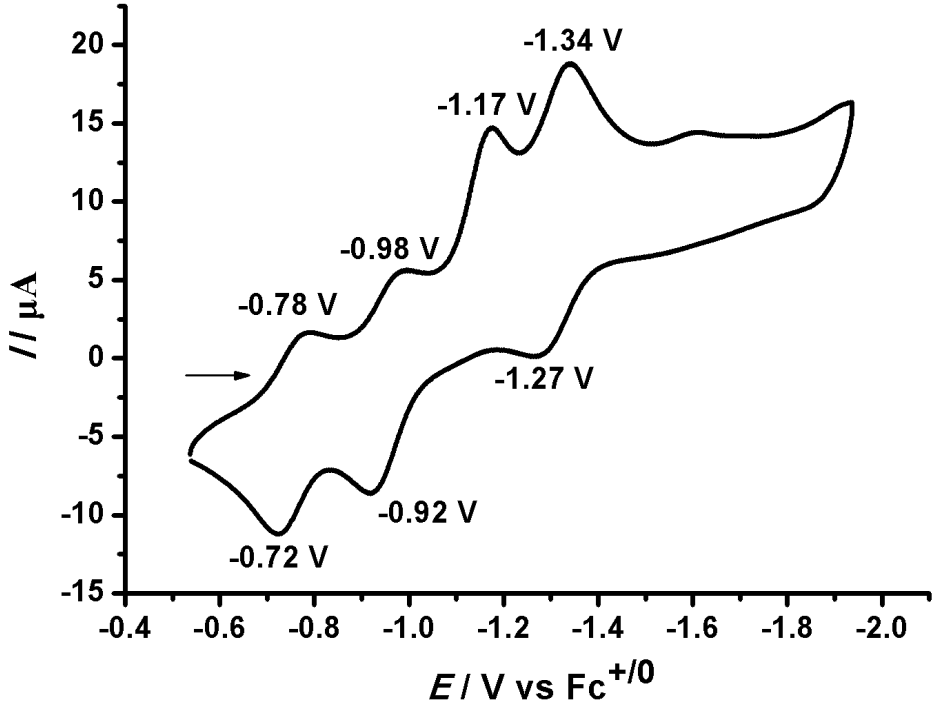

Figure S36. The cyclic voltammogram of **2[PF$_6$]$_2$** (1 mM) in 0.1 M ^{n}Bu$_4$NPF$_6$/CH$_2$Cl$_2$ at 25 °C with a scan rate of 100 mV s^{-1}

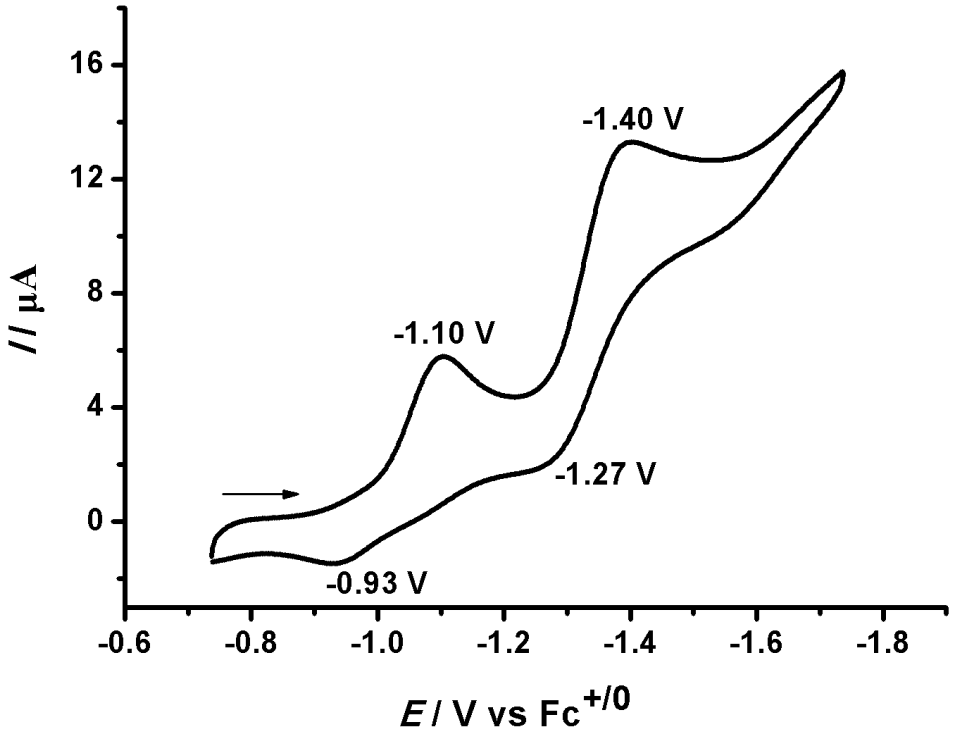

Figure S37. The cyclic voltammograms of **2[PF$_6$]$_2$** (1 mM) in 0.1 M ^{n}Bu$_4$NPF$_6$/MeCN at 25 °C at different scan rates (0.1~1.0 V s^{-1})

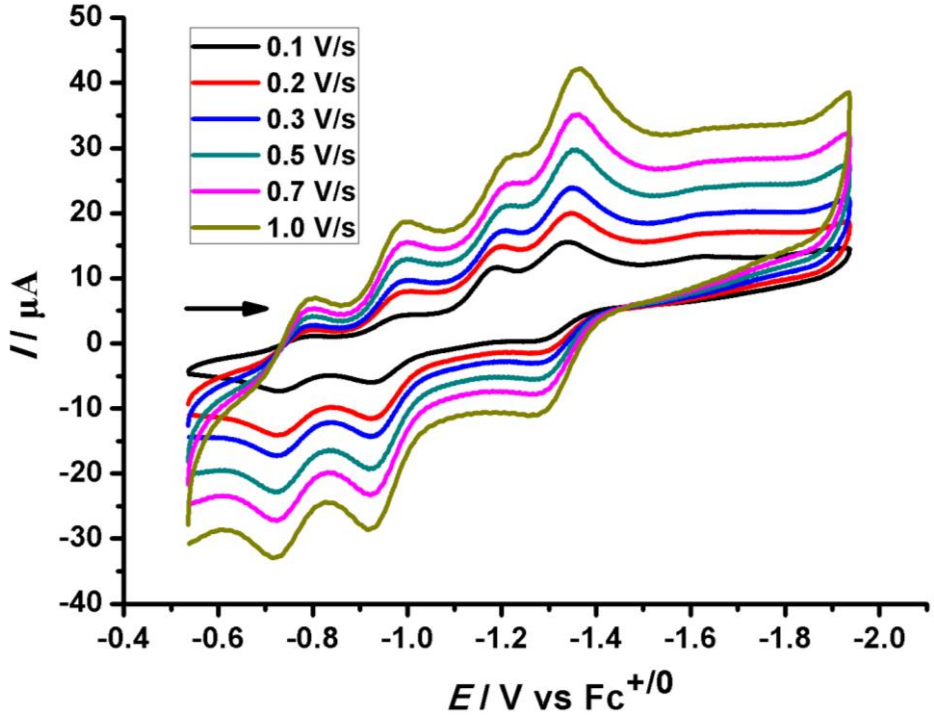

Figure S38. Plot of i_p versus $v^{1/2}$ for the third reduction peak of **2[PF$_6$]$_2$**

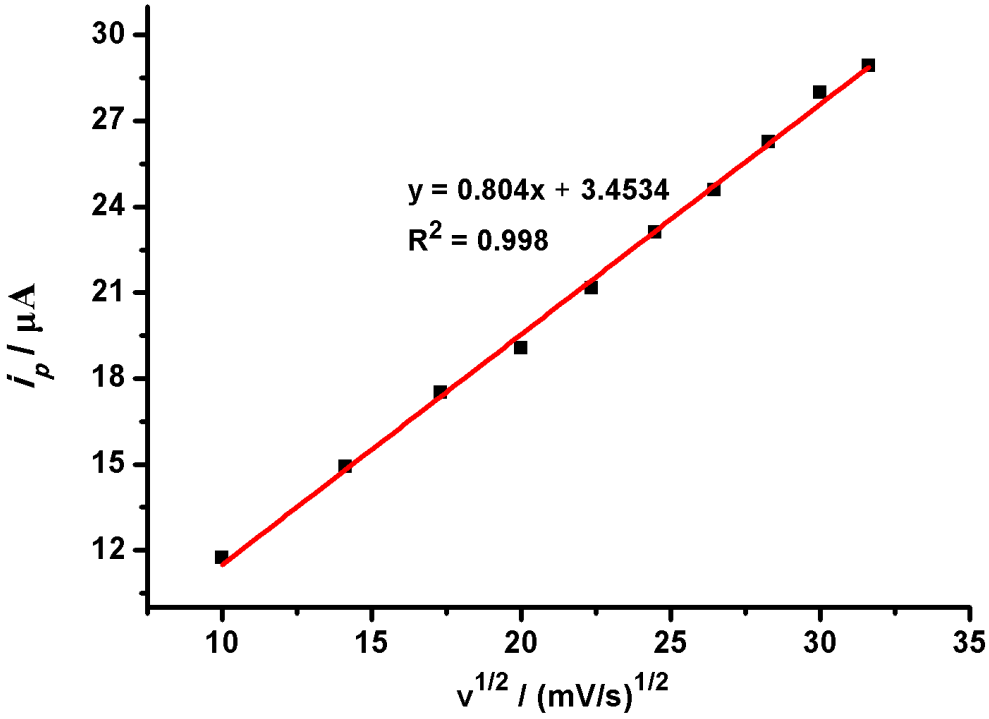

Figure S39. The cyclic voltammogram of **3[PF$_6$]** (1 mM) in 0.1 M ^{n}Bu$_4$NPF$_6$/MeCN at 25 °C with a scan rate of 100 mV s^{-1}

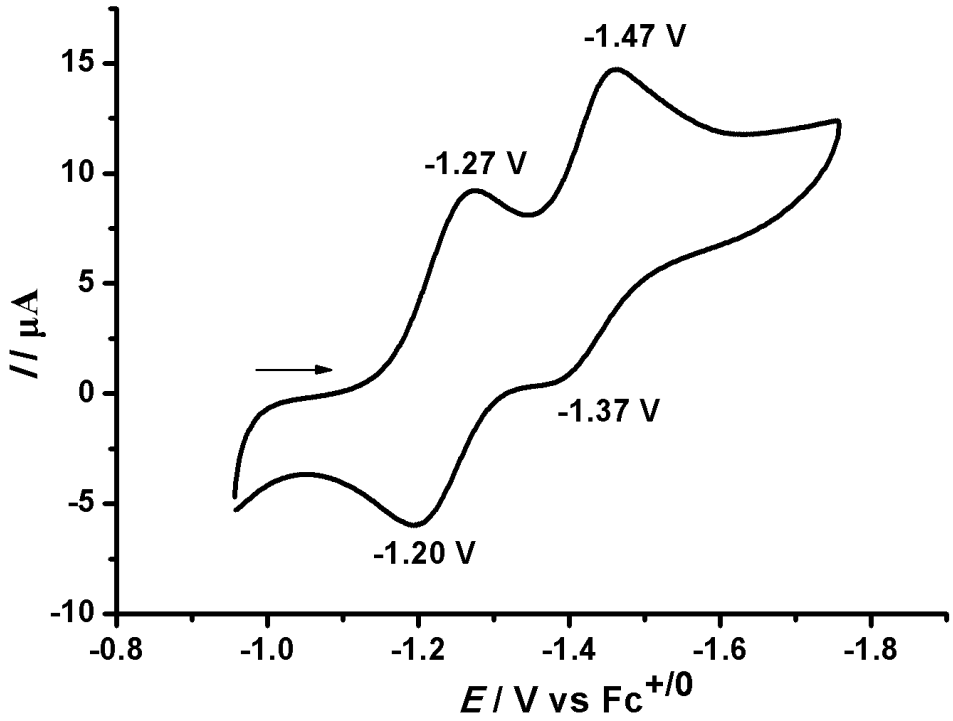

Figure S40. The cyclic voltammogram of **3[PF$_6$]** (1 mM) in 0.1 M ^{n}Bu$_4$NPF$_6$/CH$_2$Cl$_2$ at 25 °C with a scan rate of 100 mV s^{-1}

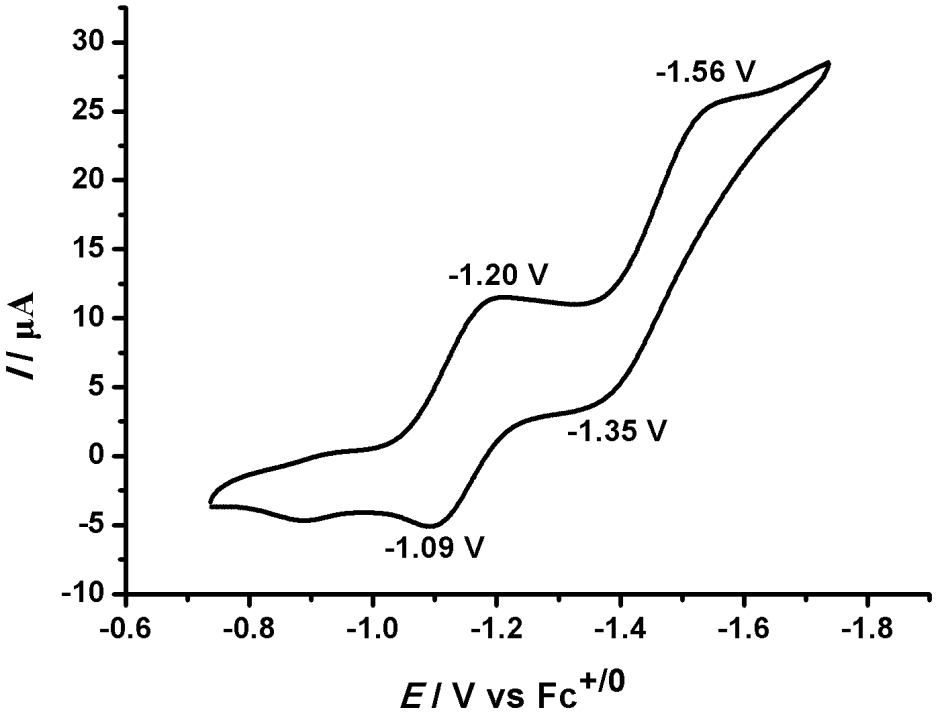

Figure S41. The cyclic voltammograms of **3[PF$_6$]** (1 mM) in 0.1 M ^{n}Bu$_4$NPF$_6$/MeCN at 25 °C at different scan rates (0.1~1.0 V s^{-1})

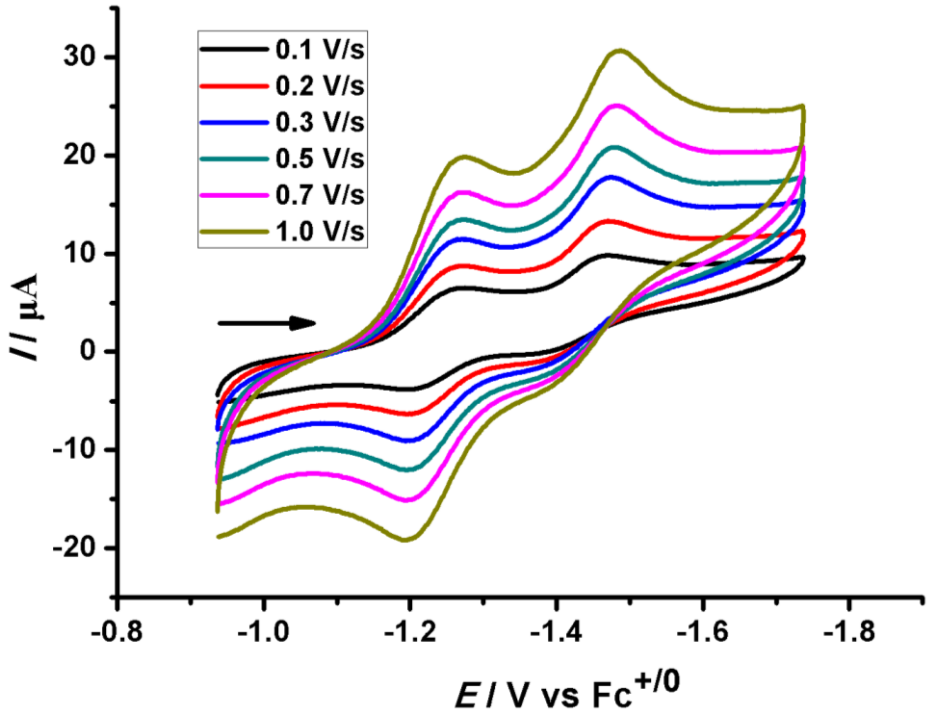

Figure S42. Plot of i_p versus $v^{1/2}$ for the second reduction peak of **3[PF$_6$]**

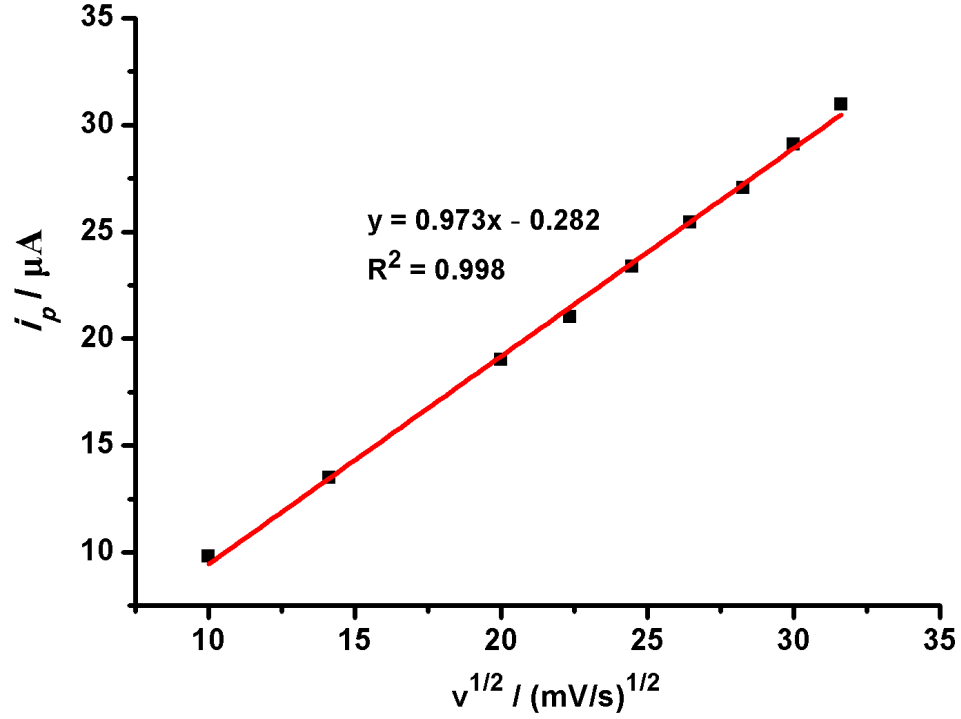

Figure S43. The cyclic voltammogram of **4[PF$_6$]** (1 mM) in 0.1 M ^{n}Bu$_4$NPF$_6$/MeCN at 25 °C with a scan rate of 100 mV s^{-1}

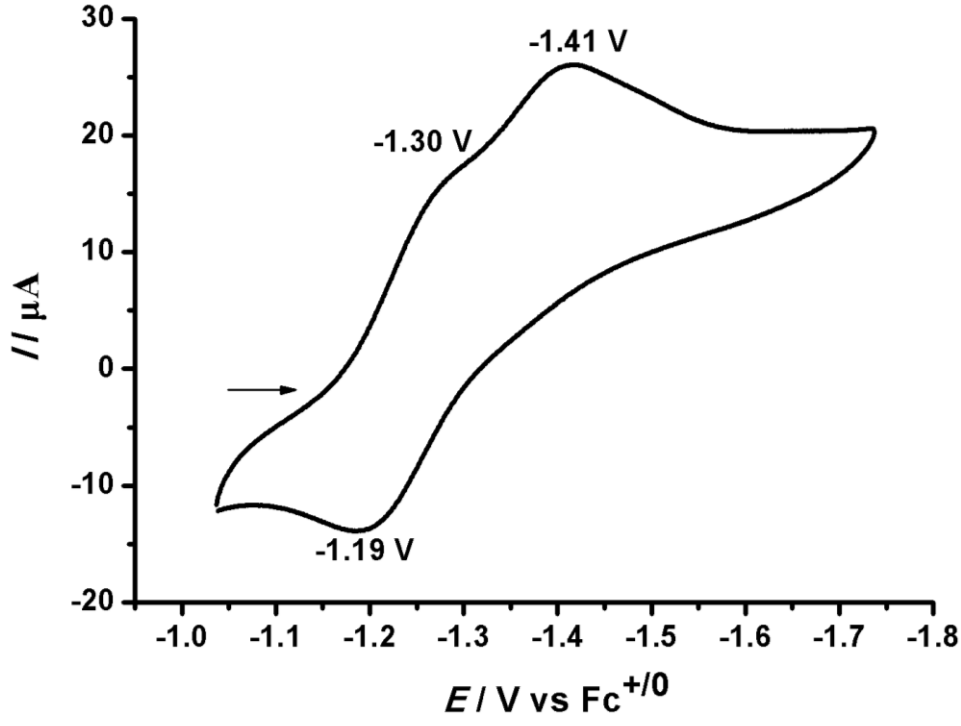

Figure S44. The cyclic voltammogram of **4[PF_6]** (1 mM) in 0.1 M $^{n}Bu_4NPF_6/CH_2Cl_2$ at 25 °C with a scan rate of 100 mV s^{-1}

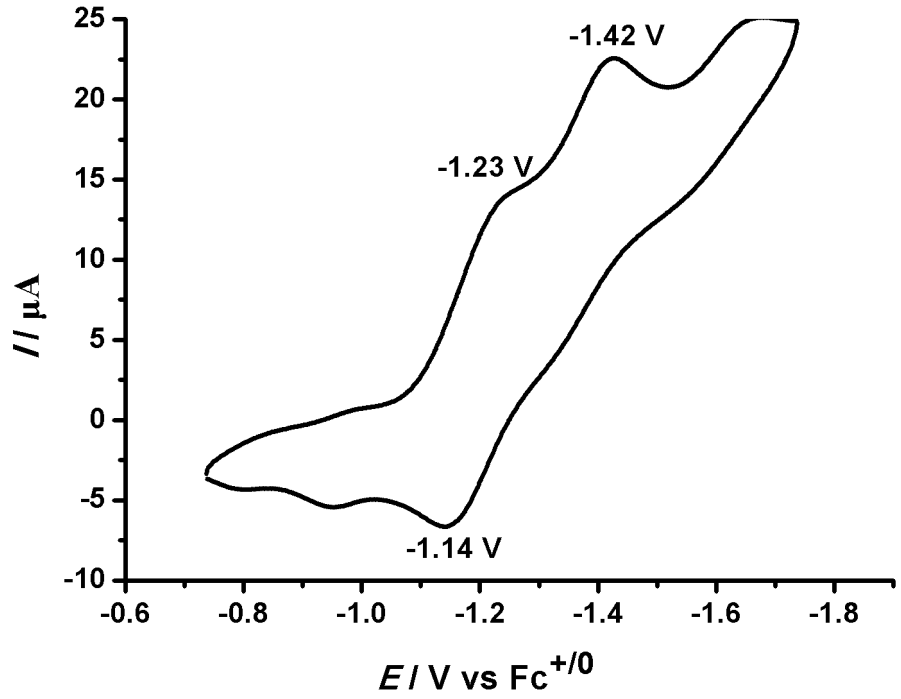

Figure S45. The cyclic voltammograms of **4[PF_6]** (1 mM) in 0.1 M $^{n}Bu_4NPF_6$/MeCN at 25 °C at different scan rates (0.1~0.7 V s^{-1})

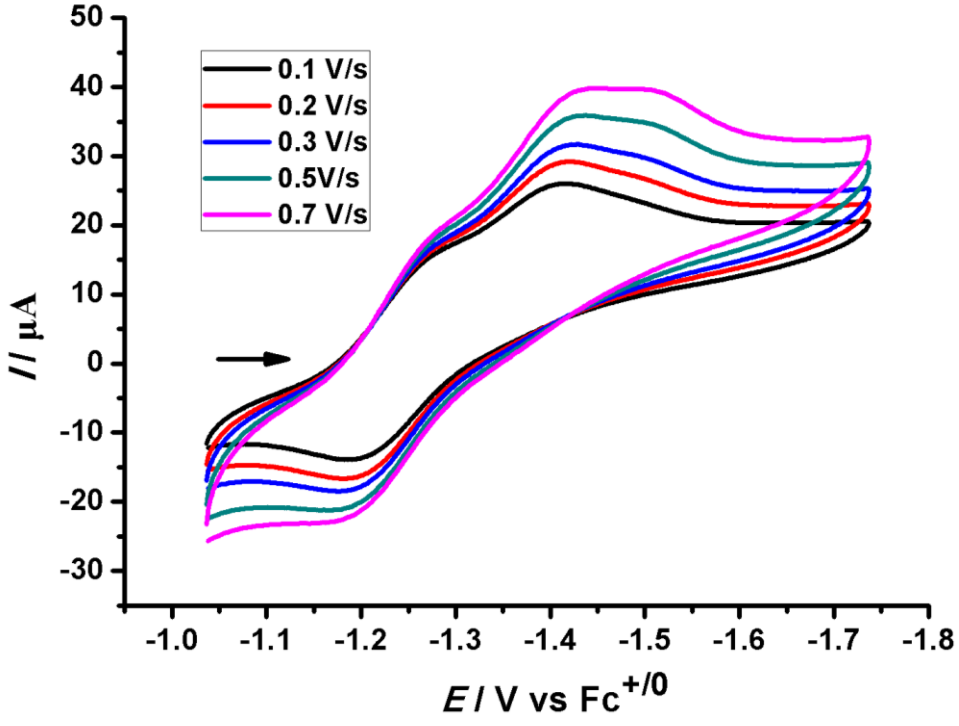

Figure S46. Plot of i_p versus $v^{1/2}$ for the second reduction peak of **4[PF$_6$]**

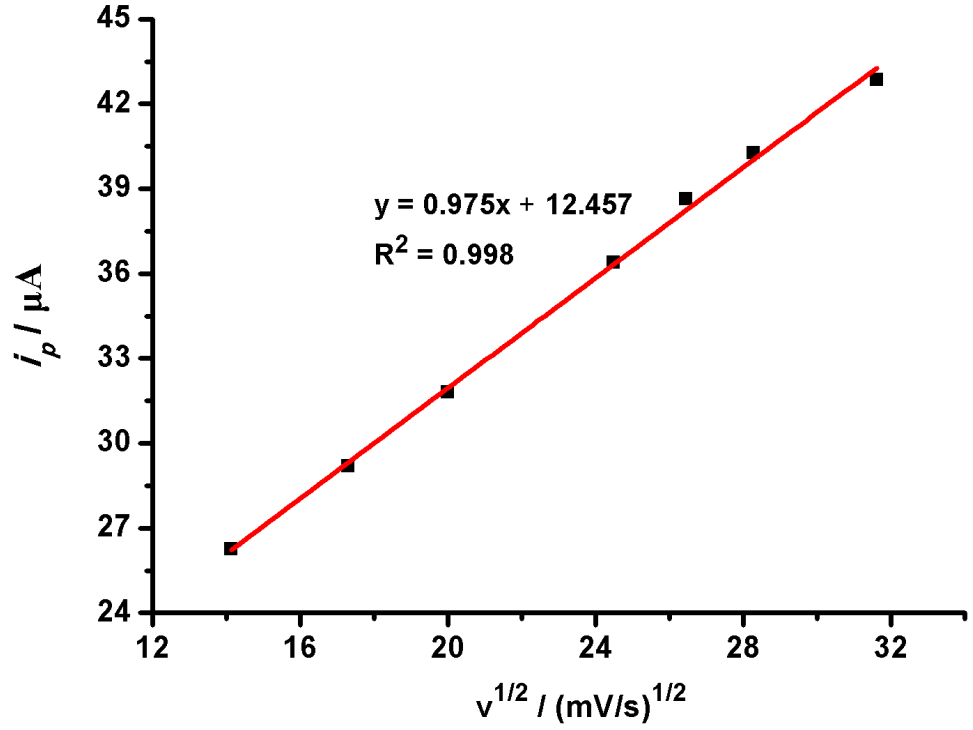

Figure S47. Cyclic voltammograms of **1[PF$_6$]$_2$** (1 mM in 0.1 M ^{n}Bu$_4$NPF$_6$ in MeCN under Ar, scan rate = 100 mV s^{-1}) with increments of TFA (0, 1, 2, 4, 6, 8 and 10 mM)

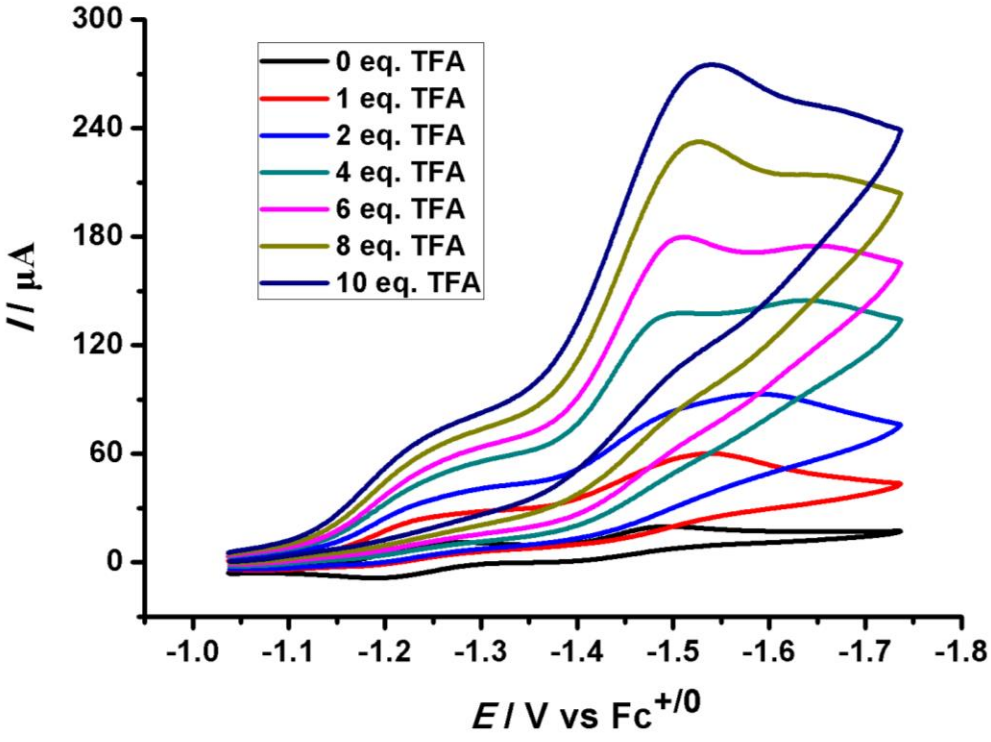

Figure S48. Corresponding plot of i_c/i_p for 1 mM **1[PF$_6$]$_2$** on the concentration of TFA near to cathodic process at −1.3 V in MeCN

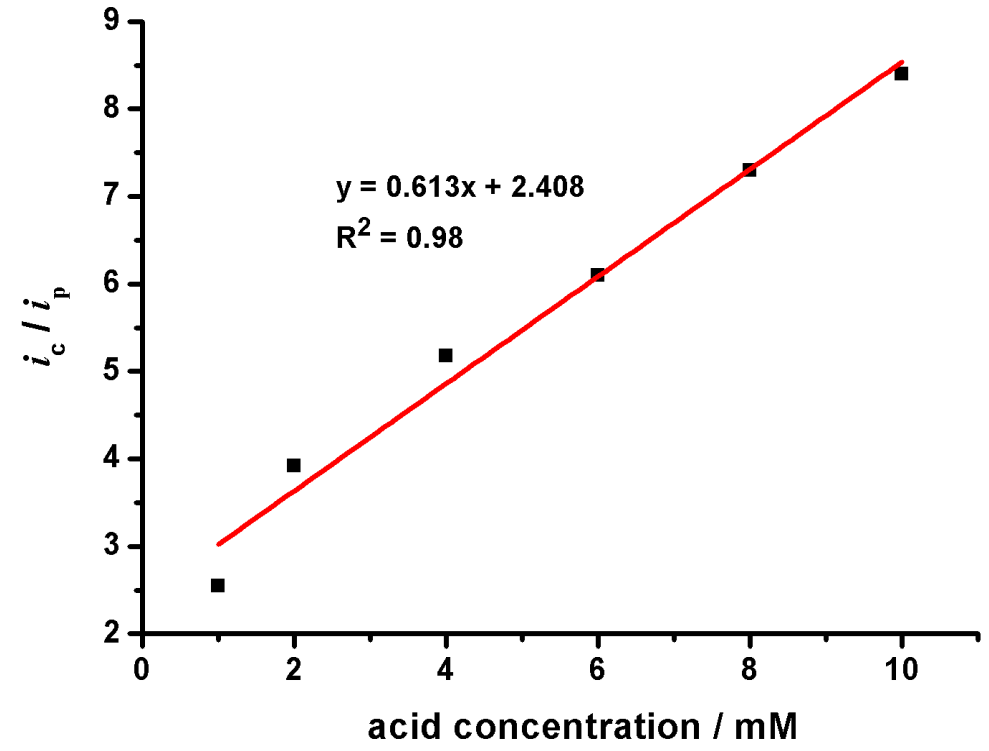

Figure S49. Cyclic voltammograms of **2[PF$_6$]$_2$** (1 mM in 0.1 M ^{n}Bu$_4$NPF$_6$ in MeCN under Ar, scan rate = 100 mV s^{-1}) with increments of TFA (0, 1, 2, 4, 8, 10, 20, 40 and 60 mM)

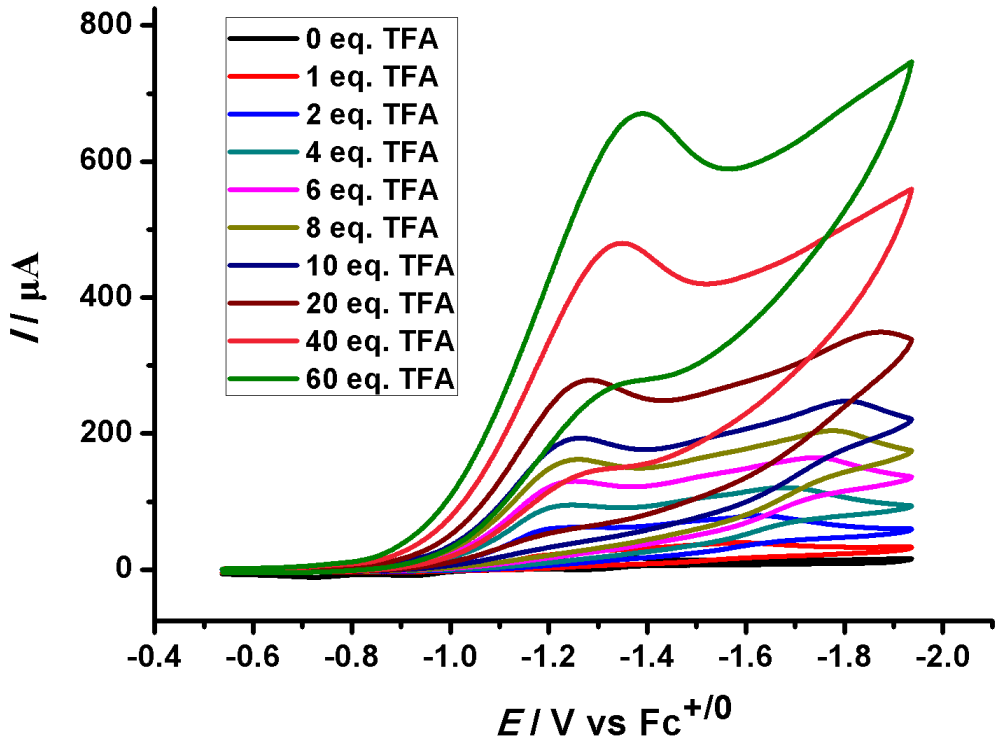

Figure S50. Corresponding plot of i_c/i_p for 1 mM **2[PF$_6$]$_2$** on the concentration of TFA near to cathodic process at −1.3 V in MeCN

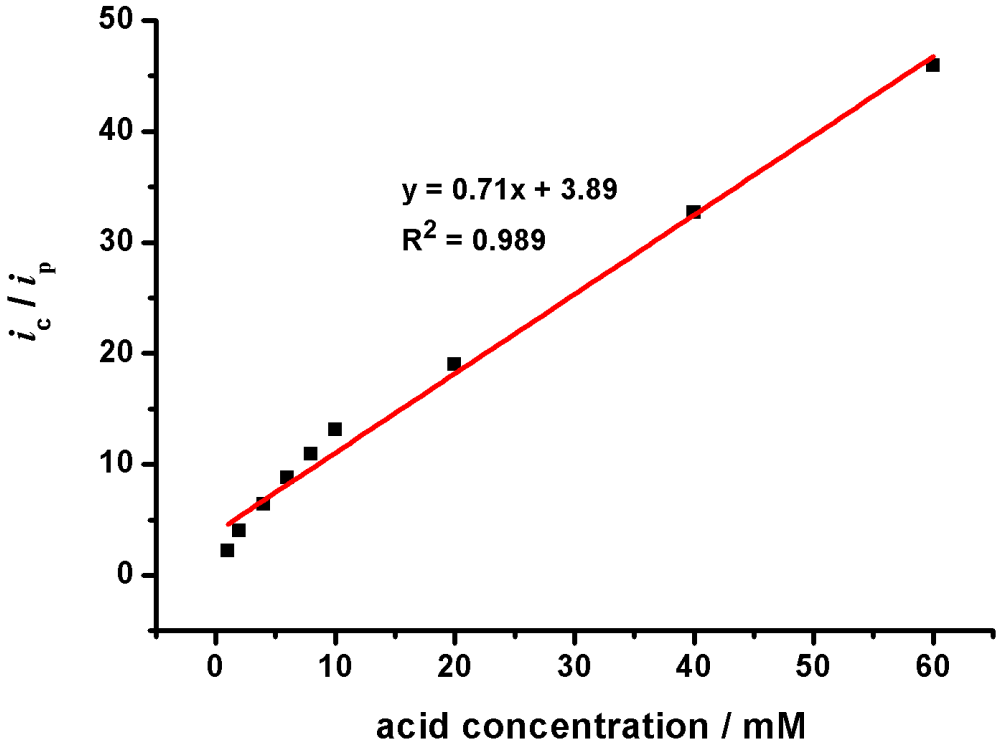

Figure S51. Cyclic voltammograms of **2[PF$_6$]$_2$** (1 mM in 0.1 M ^{n}Bu$_4$NPF$_6$ in MeCN under Ar, scan rate = 100 mV s^{-1}) with increments of TFA (0 and 2 mM)

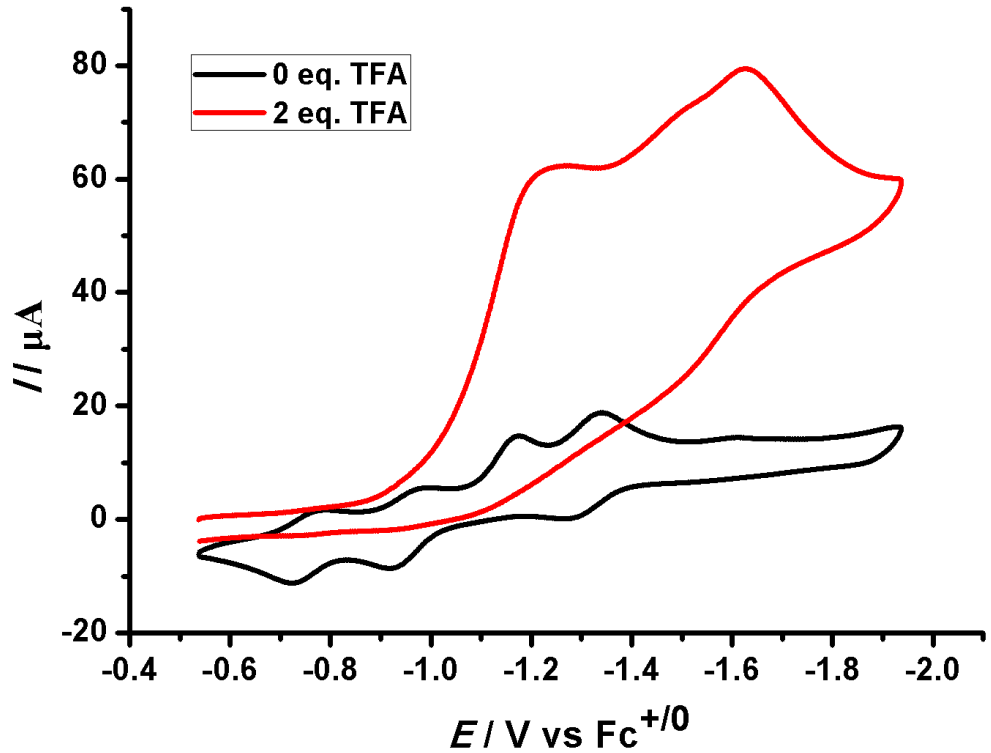

Figure S52. Cyclic voltammograms of **3[PF$_6$]** (1 mM in 0.1 M ^{n}Bu$_4$NPF$_6$ in MeCN under Ar, scan rate = 100 mV s^{-1}) with increments of TFA (0, 1, 2, 4, 6, 8 and 10 mM)

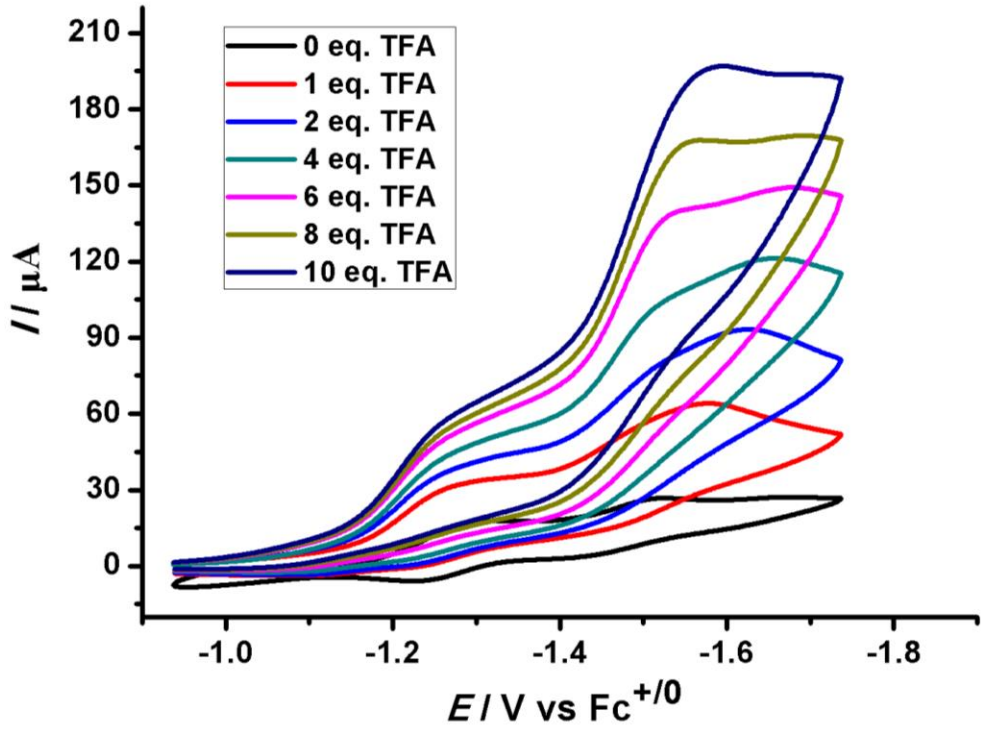

Figure S53. Corresponding plot of i_c/i_p for 1 mM **3[PF$_6$]** on the concentration of TFA near to cathodic process at −1.3 V in MeCN

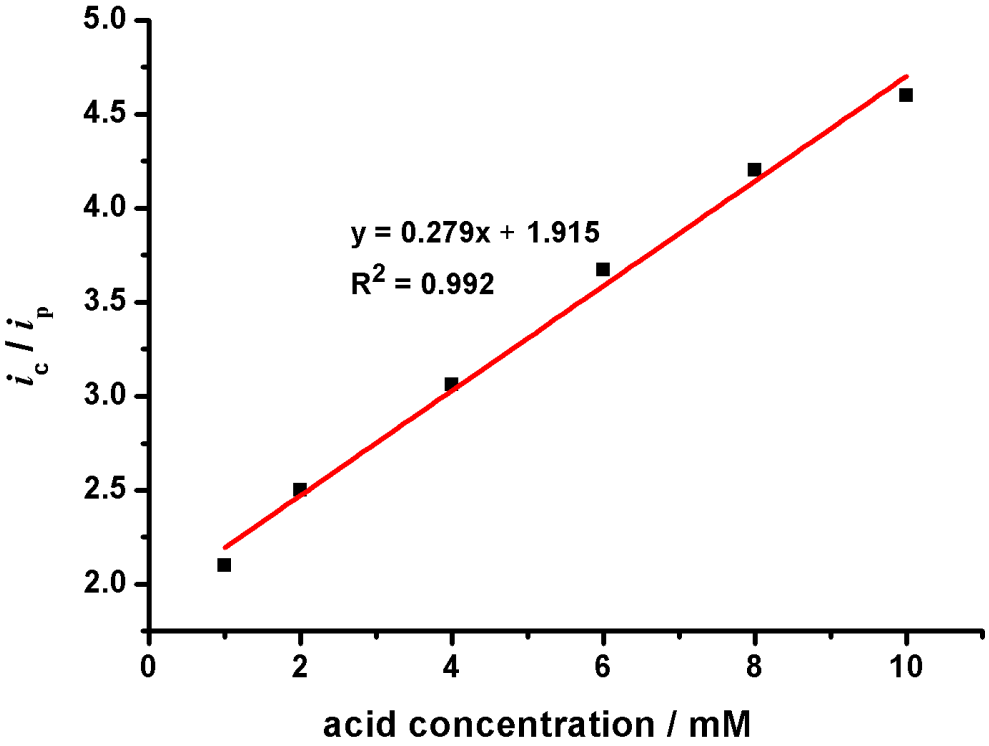

Figure S54. Cyclic voltammograms of **4[PF$_6$]** (1 mM in 0.1 M ^{n}Bu$_4$NPF$_6$ in MeCN under Ar, scan rate = 100 mV s^{-1}) with increments of TFA (0, 1, 2, 4, 6, 8, 10, 20, 30 and 40 mM)

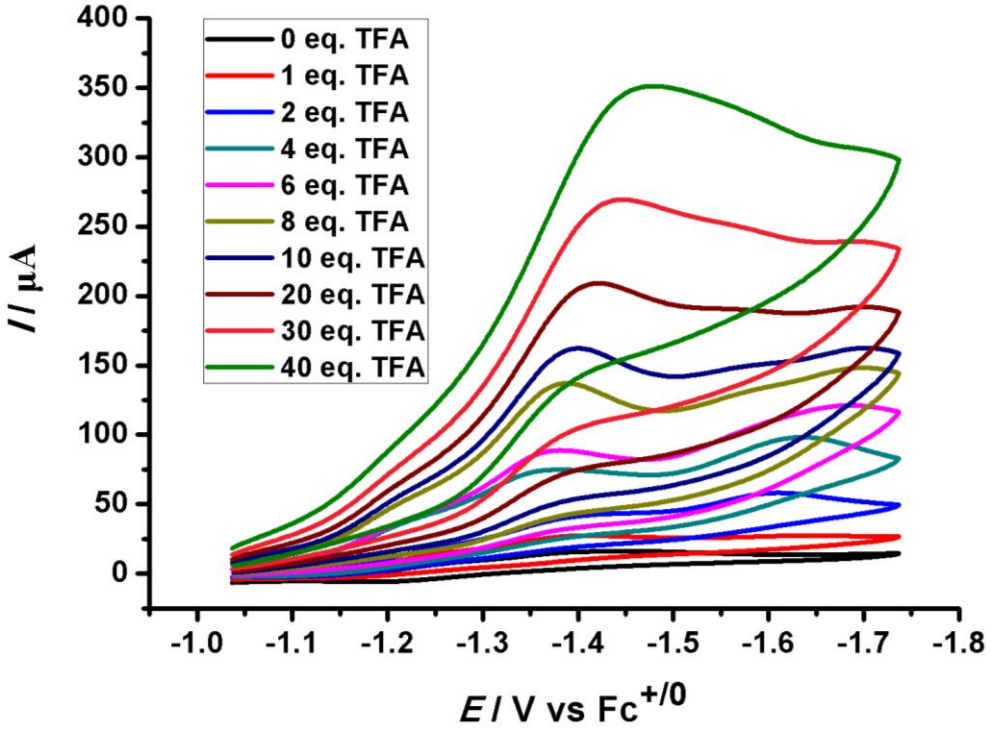

Figure S55. Corresponding plot of i_c/i_p for 1 mM **4[PF$_6$]** on the concentration of TFA near to cathodic process at −1.5 V in MeCN

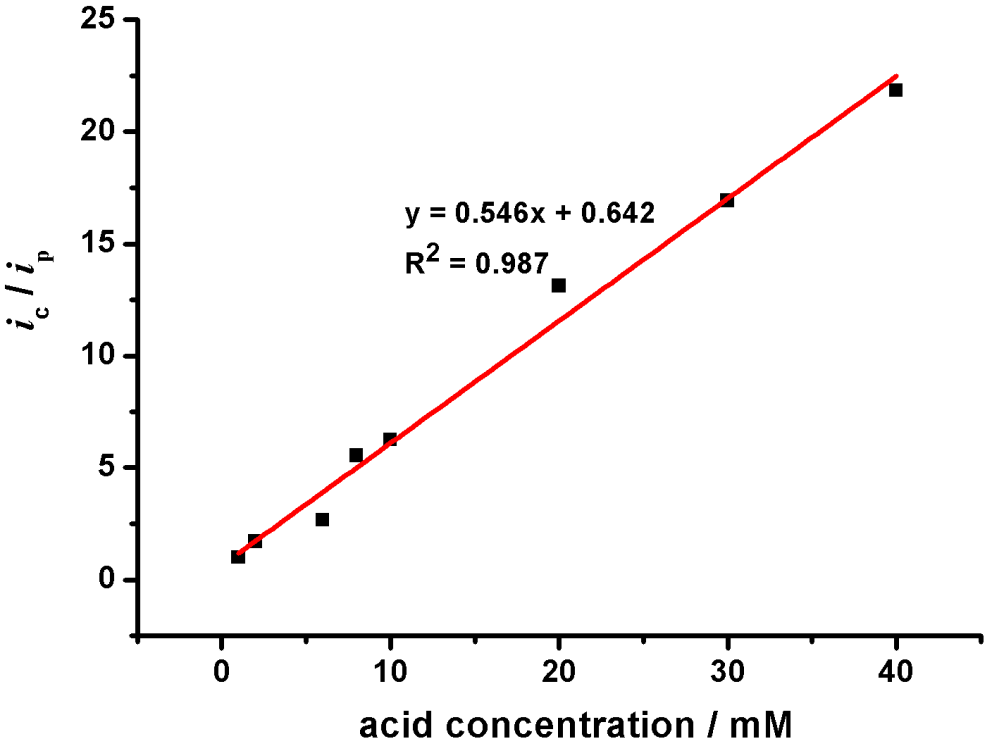

Figure S56. The cyclic voltammograms in 0.1 M $^{n}Bu_4NPF_6$/MeCN with a scan rate of 100 mV s^{-1}

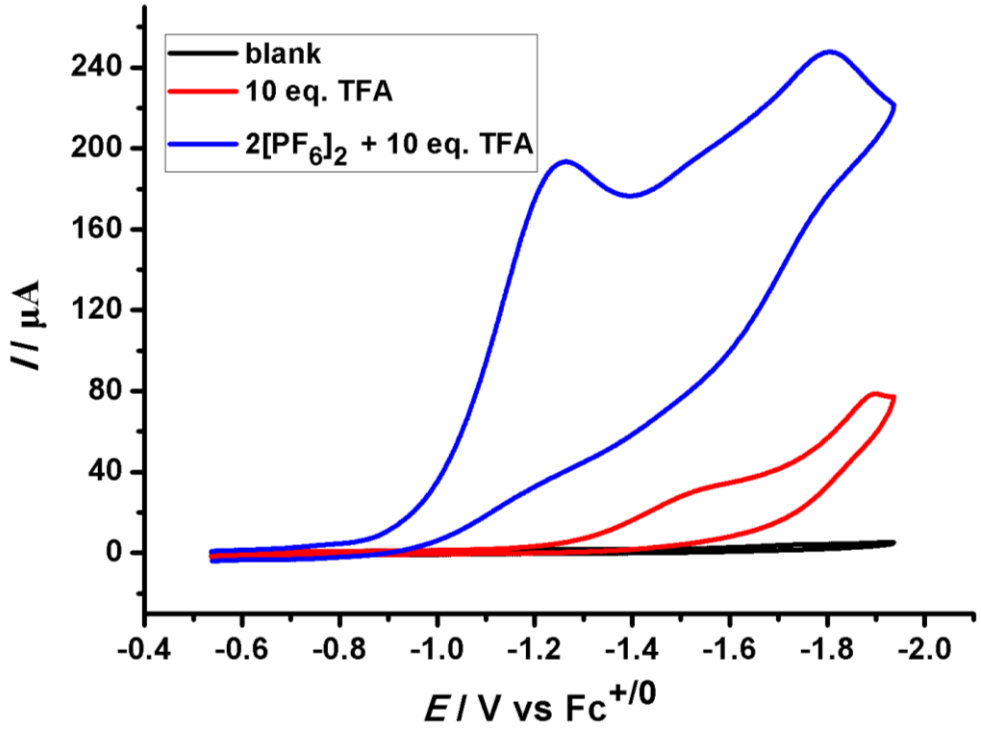

Figure S57. The i-t curve for bulk electrolysis of TFA (10 mM) in the presence of **1[PF6]2** (1 mM) at –1.3 V

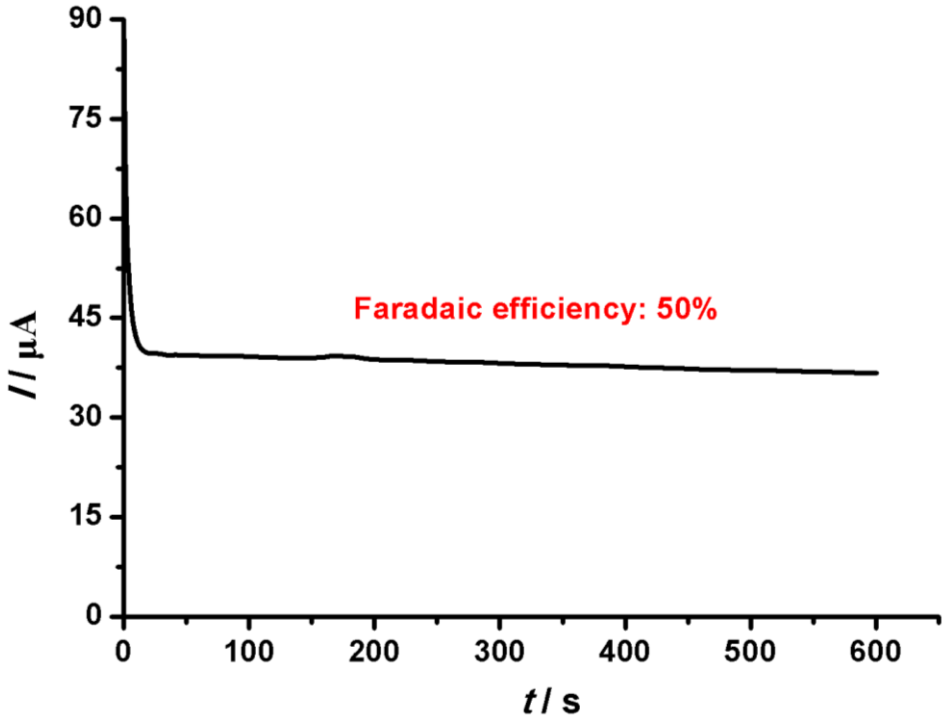

Figure S58. The i-t curve for bulk electrolysis of TFA (60 mM) in the presence of **2[PF_6]$_2$** (1 mM) at –1.2 V

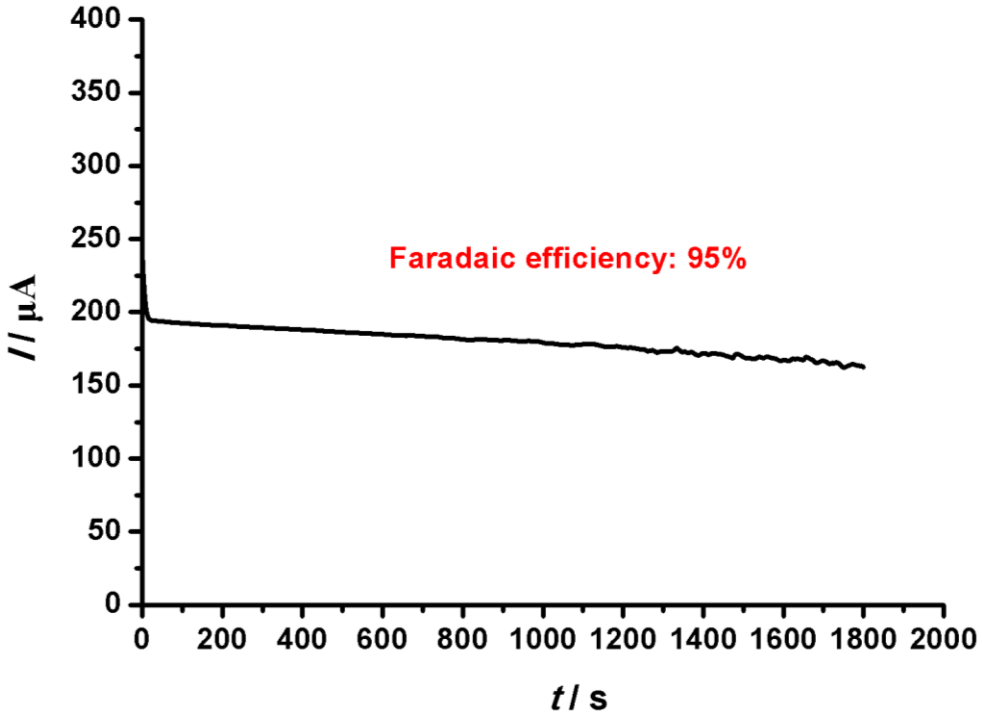

Figure S59. The i-t curve for bulk electrolysis of TFA (10 mM) in the presence of **3[PF_6]** (1 mM) at –1.3 V

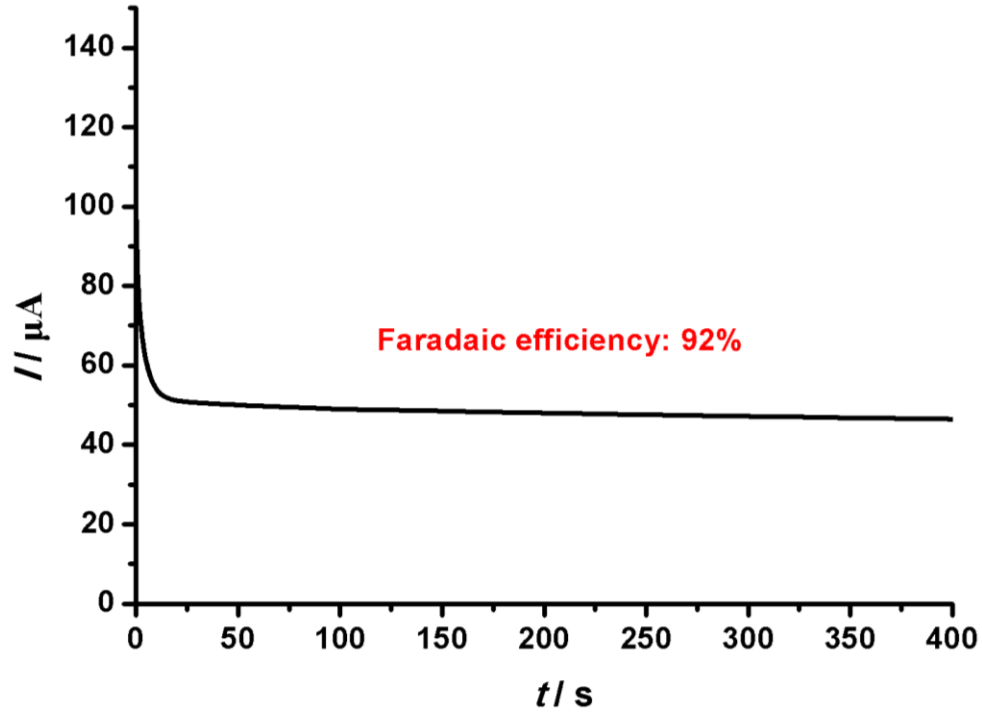

Figure S60. The i-t curve for bulk electrolysis of TFA (40 mM) in the presence of **4[PF$_6$]** (1 mM) at –1.3 V

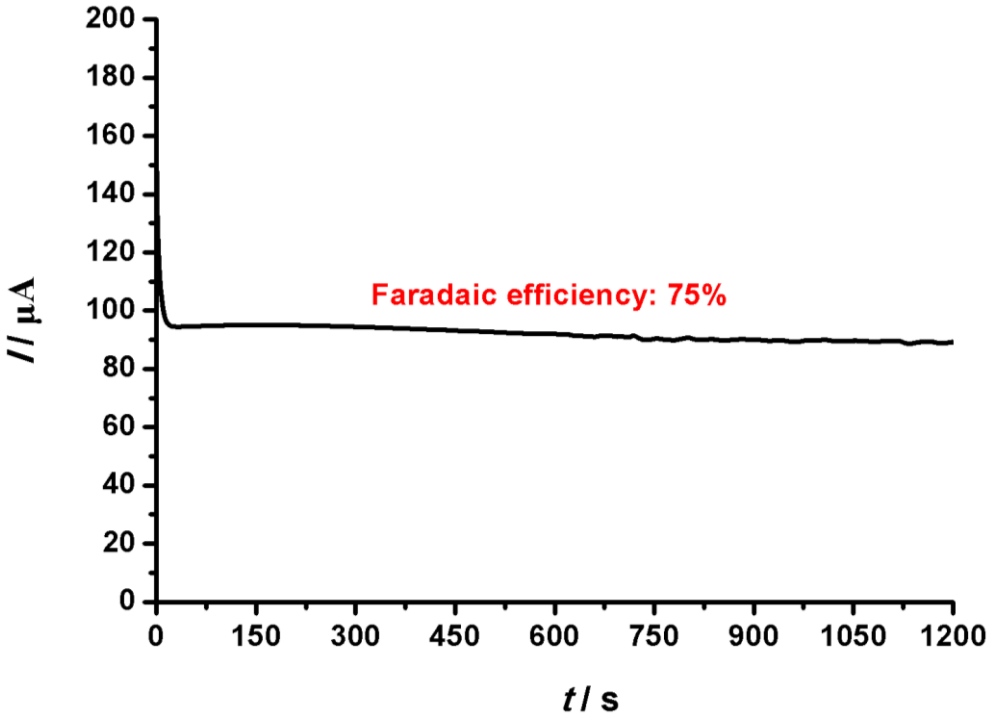

Figure S61. Cyclic voltammograms recorded for the rinse test experiments.

Detailed procedure: **1)** Conduct the CV scan of 1 mM of complex **2[PF$_6$]$_2$** in a MeCN solution containing 0.1 M ^{n}Bu$_4$NPF$_6$ and 10 mM TFA; **2)** The solution was then discarded and the electrodes were rinsed several times with pure MeCN. The electrodes were then dipped into a fresh MeCN solution containing 0.1 M ^{n}Bu$_4$NPF$_6$ and 10 mM TFA in the absence of complex **2[PF$_6$]$_2$**; **3)** Another 10 mM of TFA was added into this solution to make up 20 mM of acid while retaining the same concentrations for 0.1 M ^{n}Bu$_4$NPF$_6$; **4)** 1 mM of complex **2[PF$_6$]$_2$** was added into the solution.

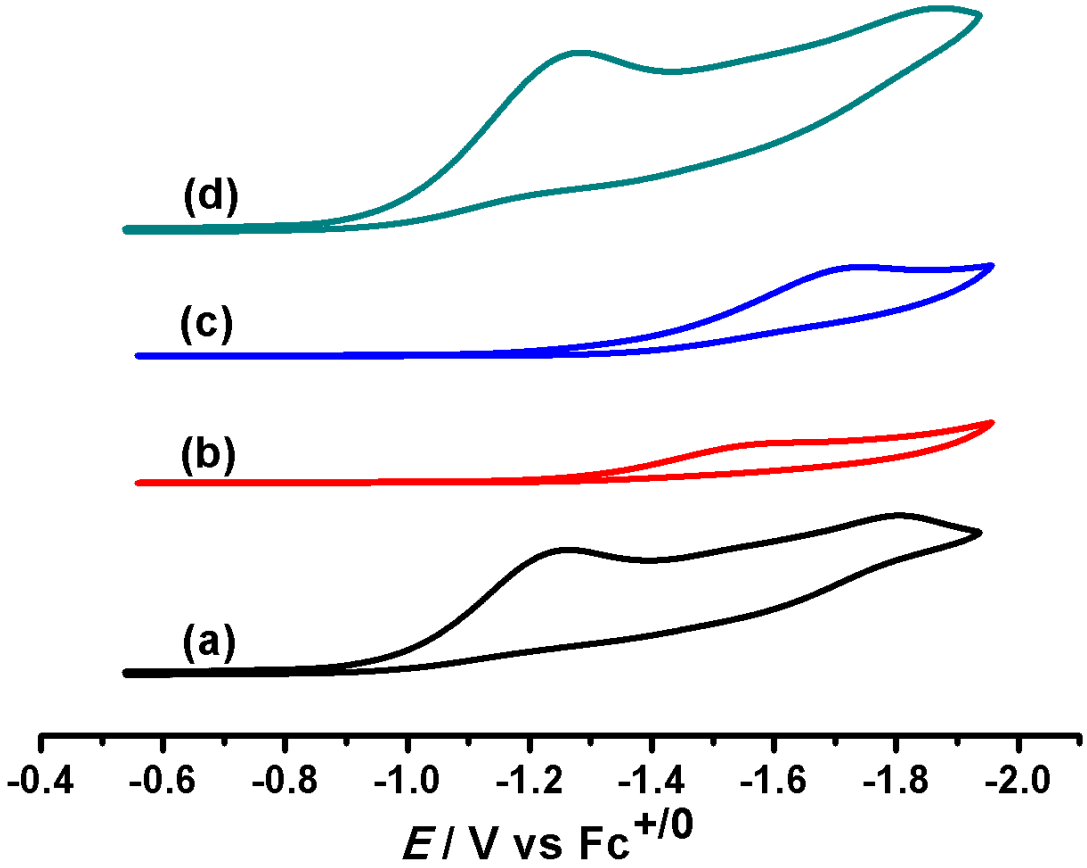

Curve (a): CV scan of 1 mM of complex **2[PF$_6$]$_2$** in a MeCN solution containing 0.1 M ^{n}Bu$_4$NPF$_6$ and 10 mM TFA. **Curve (b)**: CV scan of a fresh MeCN solution containing 0.1 M ^{n}Bu$_4$NPF$_6$ and 10 mM TFA in the absence of complex **2[PF$_6$]$_2$**. **Curve (c)**: CV scan of the solution containing 20 mM of TFA in the absence of complex **2[PF$_6$]$_2$**. **Curve (d)**: CV scan of the solution containing **2[PF$_6$]$_2$** and 20 mM of TFA.

Determine the amount of H_2

Choose catalyst **2[PF_6]$_2$** as an example. Firstly, we constructed a standard curve based on the relationship between peak area and amount of hydrogen by gas chromatography (GC), as shown **Figure 62a**. After bulk electrolysis, 1 mL of gas sample was extracted from headspace (30 mL) of H-type electrolysis cell using gas-tight syringe and then injected into GC instrument. An obvious signal peak for hydrogen appeared at the retention time of 0.597 min (**Figure 62b**), which can be integrated to give the value of the peak area. Finally, this value was brought into the above standard curve of hydrogen to obtain the amount of hydrogen.

***Figure S62*. (a)** Standard curve of hydrogen **(b)** GC plot of gas analysis of headspace

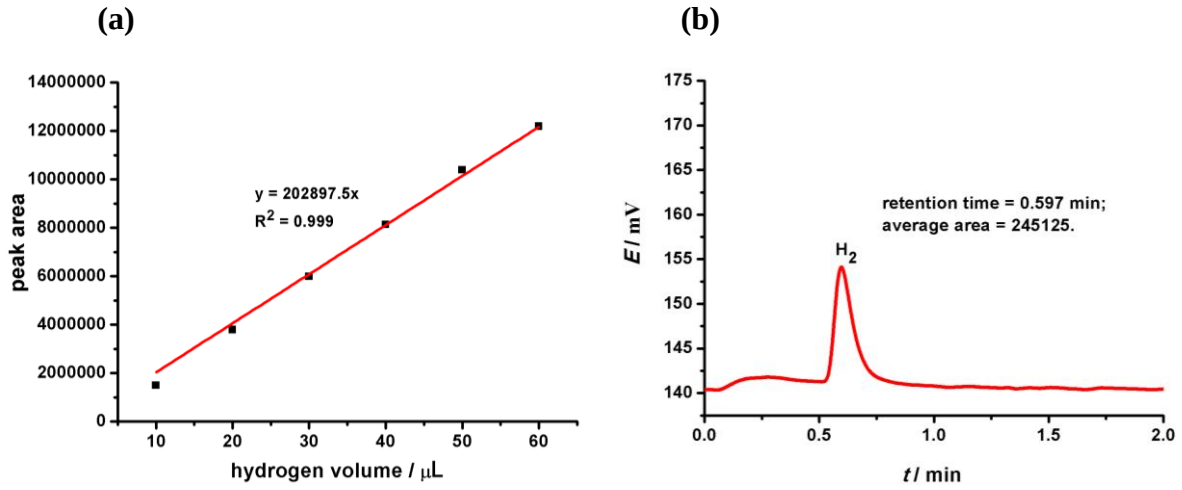

Overpotential determinations

For many acids, homoconjugation of acid/base pairs is a known problem, which significantly lowers the accuracy of calculating E^0_{HA}. TFA has a relatively large homoconjugation constant in MeCN.[1] E^0_{HA} has been accurately measured by Artero and coworkers by taking into account homoconjugation of the acid at various concentrations.[2] For 10 mM TFA, E^0_{HA} = –0.68 V versus $Fc^{+/0}$. Now that we can have determined a value for E^0_{HA}, we can calculate the overpotential for the reduction of H^+ to H_2 via eq. S1.

$$\text{Overpotential} = |E^0_{HA} - E_{cat/2}| \qquad \text{eq. S1}$$

In the eq. S1, the catalytic potential is defined as the potential at half of the catalytic current ($E_{cat/2}$), as recommended by Appel and Helm.[3]

Figure S63. Determinations of the overpotential of complexes **1[PF6]2**, **2[PF6]2**, **3[PF6]** and **4[PF6]** for hydrogen evolution from TFA (10 mM) in MeCN.

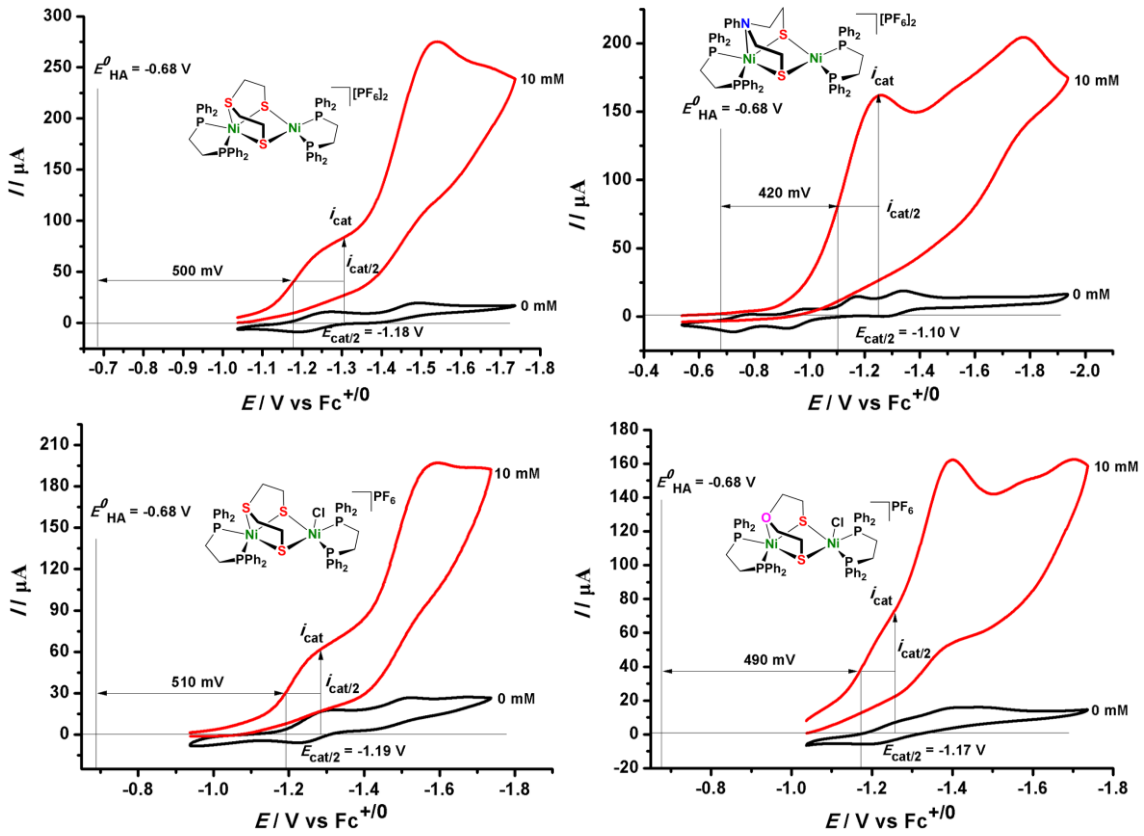

References

1 K. Izutsu, *Acid-Base Dissocation Constants in Dipolar Aprotic Solvents*; Blackwell Scientific Publications: Oxford, Boston, 1990.

2 V. Fourmond, P.-A. Jacques, M. Fontecave and V. Artero, *Inorg. Chem.*, 2010, **49**, 10338-10347.

3 A. M. Appel and M. L. Helm, *ACS Catal.*, 2014, **4**, 630-633.